2019

Calibration of structured light system using unidirectional fringe patterns

Vignesh Suresh
Iowa State University

Calibration of structured light system using unidirectional fringe patterns

by

Vignesh Suresh

A thesis submitted to the graduate faculty

in partial fulfillment of the requirements for the degree of

MASTER OF SCIENCE

Major: Mechanical Engineering

Program of Study Committee:
Beiwen Li, Major Professor
James H Oliver
Abhijit Chandra

The student author, whose presentation of the scholarship herein was approved by the program of study committee, is solely responsible for the content of this thesis. The Graduate College will ensure this thesis is globally accessible and will not permit alterations after a degree is conferred.

Iowa State University

Ames, Iowa

2019

DEDICATION

I would like to dedicate this thesis to my mom, dad and sister.

TABLE OF CONTENTS

Page

LIST OF TABLES

Page

LIST OF FIGURES

Page

ACKNOWLEDGMENTS

I would like to take this as an opportunity to thank all the people who have helped me in my research. First and foremost, Dr. Beiwen Li for giving me an opportunity to work with him and the patience with which he explained all the concepts related to the research domain. I would like to thank him on a special note for his considerate approach. The interactions with him made me gain so much knowledge in this research field. Overall, it is a great experience working in his lab. Also, I would like to thank my committee members Dr. Jim Oliver and Dr. Abhijit Chandra for accepting my request to be on my committee.

Last but not least, I would like to thank my parents without whom I could not have completed this work.

ABSTRACT

3D shape measurement has a variety of applications in many areas, such as manufacturing, design, medicine and entertainment. There are many technologies that were successfully implemented in the past decades to measure three dimensional information of an object. The measurement techniques can be broadly classified into contact and non-contact measurement methods. One of the most widely used contact method is Coordinate Measuring Machine (CMM) which dates back to late 1950s. The method by far is one of the most accurate method as it can have sub-micrometer accuracy. But it becomes difficult to use this technique for soft objects as the probe might deform the surface of the object being measured. Also the scanning could be a time-consuming process.

In order to address the problems in contact methods, non-contact methods such as time of flight (TOF), triangulation based laser scanner techniques, depth from defocus and stereo vision were invented. The main limitation with the time of flight laser scanner is that it does not give a high depth resolution. On the other hand, triangulation based laser scanning method scans the object line by line which might be time consuming. The depth from defocus method obtains 3D information of the object by relating depth to defocus blur analysis. However, it is difficult to capture the 3D geometry of objects that does not have a rich texture. The stereo vision system imitates human vision. It uses two cameras for capturing pictures of the object from different angles. The 3D coordinate information is obtained using triangulation. The main limitation with this technology is: when the object has a uniform texture, it becomes difficult to find corresponding pairs between the two cameras. Therefore, the structured light system (SLS) was introduced to address the above mentioned limitations.

SLS is an extension of stereo vision system with one of the cameras being replaced by a projector. The pre-designed structured patterns are projected on to the object using a video projector. The main advantage with this system is that it does not use the object's texture for identifying the

corresponding pairs. But the patterns have to be coded in a certain way so that the camera-projector correspondence can be established. There are many codifications techniques such as pseudo-random codification, binary and N-ary codification. Pseudo-random codification uses laser speckles or structure-coded speckle patterns that vary in both the directions. However, the resolution is limited because each coded structure occupies multiple pixels in order to be unique. On the other hand, binary codifications projects a sequence of binary patterns. The main advantage with such a codification is that it is robust to noise as only two intensity levels are used (0s and 255). However, the resolution is limited because the width of the narrowest coding stripe should be more than the pixel size. Moreover, it takes many images to encode a scene that occupies a large number of pixels. To address this, N-ary codification makes use of multiple intensity levels between 0 and 255. Therefore the total number of coded patterns can be reduced. The main limitation is that the intensity-ratio analysis may be subject to noise.

Digital Fringe Projection (DFP) system was developed to address the limitations of binary and N-ary codifications. In DFP computer generated sinusoidal patterns are projected on to the object and then the camera captures the distorted patterns from another angle. The main advantage of this method is that it is robust to the noise, ambient light and reflectivity as phase information is used instead of intensity. Albeit the merit of using phase, to achieve highly accurate 3D geometric reconstruction, it is also of crucial importance to calibrate the camera-projector system. Unlike the camera calibration, the projector calibration is difficult. This is mainly because the projector cannot capture images like a camera. Early attempts were made to calibrate the camera-projector system using a reference plane. The object geometry was reconstructed by comparing the phase difference between the object and the reference plane. However, the chosen reference plane needs to simultaneously possess a high planarity and a good optical property, which is typically difficult to achieve. Also, such calibration may be inaccurate if non-telecentric lenses are used. Calibration of the projector can also be done by treating it as the inverse of a camera. This method addressed the limitations of reference plane based method, as the exact intrinsic and extrinsic parameters of the imaging lenses are obtained. So a perfect reference plane is no longer required. The calibration

method typically requires projecting orthogonal patterns on to the object. However, this method of calibration can be used only for structured light system with video projector. Grating slits and interferometers cannot be calibrated by this method as we cannot produce orthogonal patterns with such systems.

In this research we have introduced a novel calibration method which uses patterns only in a single direction. We have theoretically proved that there exists one degree-of-freedom of redundancy in the conventional calibration methods, thus making it possible to use unidirectional patterns instead of orthogonal fringe patterns. Experiments show that under a measurement range of $200mm \times 150mm \times 120mm$, our measurement results are comparable to the results obtained using conventional calibration method. Evaluated by repeatedly measuring a sphere with 147.726 mm diameter, our measurement accuracy on average can be as high as 0.20 mm with a standard deviation of 0.12 mm.

CHAPTER 1. INTRODUCTION

This chapter is a general introduction for the entire thesis. The motivation for this research is discussed in section 1.1. The contemporary and past 3D shape measurement techniques are discussed in section 1.2. The objective of the research is discussed in section 1.4. Finally, the structure of the thesis is discussed in section 1.5.

1.1 Overview

The imaging technology has gained so much importance in the recent times and it is evident from the extensive research that is happening in this field. This is mainly because of its potential applications in many diverse fields. In today's world the imaging technology is used in almost all fields including high speed cameras accurately tracking the motion of a cricket ball; doctors using an endoscopy machine to see the interior organs of humans; cameras that are installed in hallways for surveillance purposes. So a 3D image is more desirable than 2D in the above mentioned scenarios in order to make accurate decisions as the planar information is not sufficient. In order to obtain an accurate 3D information of the scene the system needs to be calibrated. The dimensional inaccuracies can be reduced with a precise calibration system.

3D imaging is widely used in many fields. Some example applications are elaborated as follows.

1.1.1 Medicine and Biology

Imaging techniques have been widely used in the area of medicine. The complicated surgeries have become less risky because of the advancements in imaging technologies. Doctors are able to locate the interior damage accurately with the help of advanced imaging techniques like endoscopy, computed tomography (CT) scan and magnetic resonance imaging (MRI). Endoscopy uses a flexible tube with a light source and camera which is inserted into the intestine to capture pictures.

Certain surgical procedures like laparascopy is possible only because of the improvement in imaging technology. Optical techniques coupled with machine learning is also used for diagnosing cancer (Devi et al., 2016). Recently, research has also been conducted on 3D endoscopy imaging techniques. One of the well known approach is to use a stereo vision system (Dhond and Aggarwal, 1989) to produce a 3D image. Apart from 3D endoscopy, imaging is also used to obtain 3D facial expressions which will be extremely helpful for cosmetic surgeries (Mehta et al., 2008). Bhatia et al. (Bhatia et al., 1994) has developed a structured light scanner using projectors and digital cameras which gives a 360 degree surface scan of the human head. This result can be used for assessing the change after a cosmetic surgery. Scientists have also been doing extensive research to visualize the functioning of heart accurately. The reason is, doctors will be able to perform more effective cardiac disease diagnosis if they can see the functioning of the cardiac system. Structured light scanning has proved in a variety of situations that it can be a good option for scanning the heart. Laughner et al. (Laughner et al., 2012) has developed an ultrafast structured light 3D imaging system with a spatial resolution of 87 μm to analyze the dynamics of a live rabbit heart. 3D imaging technique along with non-rigid motion tracking algorithm is used to track the motion of cardiac system. Apart from topological analysis, 3D imaging will be also extremely useful for doctors to diagnose potential problems in heart valve. Iyengar et al. (Iyengar et al., 2001) has developed an imaging system to track the motion of the valve leaflet. The imaging system involves projecting of 150-200 laser light points over the leaflet surface and a stereo system with high resolution boroscopes to track the laser light points. All aforementioned technological advancements have demonstrated the importance of 3D imaging in the field of medicine and biology.

1.1.2 Industrial applications

Manufacturing industries will benefit a lot from 3D imaging technologies especially in the production and quality control departments. Many industries such as automotive and aerospace industries, will require high precision in the components being made. The conventional technique used in most of the industries for 3D surface measurement is a coordinate measuring machine (CMM)

(to be discussed in section 1.2.1). CMM is widely used because of its ability to reach accuracy in sub-micrometer level. But its point by point contact nature takes a lot of time for a single measurement. One more requirement for these industries is that they will have to maintain their production volume. In such cases, the time spent on inspection should be less to maintain the production rate. On the other hand, the inspection should also be accurate. With such need, the structured light technology can be a potential solution for in-situ inspection given its combined speed and accuracy advantage.

1.1.3 Entertainment

The applications of structured light technology is not only limited to manufacturing and medicine industry. Entertainment industry also benefits a lot from the same. For instance, the first generation of Microsoft Kinect, uses structured light technology for constructing the 3D image (Villaroman et al., 2011). Many games use Kinect's algorithm to decode the gestures made by humans. The entertainment experience in video games becomes even more exciting when one can use their body parts (using a 3D structured light sensor) for playing the game instead of a hardware device controlling your motions.

1.2 Current practices

There are a variety of 3D measurement methods. They are mainly classified into two categories: (i) contact method and, (ii) non-contact method. The strength and weaknesses of each method is discussed as follows:

1.2.1 Contact method

Coordinate measuring machine is the one of the most widely used measurement technique for contact based measurements (Pettersson, 2009). CMM is a device that senses the geometry of the objects with the help of a movable probe. The probe is allowed to move in all the three axes (X, Y and Z). Each axis has a sensor for monitoring the probe in that axis. When the probe comes

in contact with a particular location on the sample being measured, then the machine will record the coordinates from the three position sensors. The probe is generally spherical in shape, few enhancements were made to its design by introducing two bar like members on to the sphere (May and Gosselin, 1986). The robotic arm that contains the probe has 6 degrees of freedom (Bailey, 2010). CMM is widely used in manufacturing industries to ensure the dimension of the parts before going into assembly. CMM has high dimensional measurement accuracies in sub-micrometer level. There are few disadvantages in using CMM and they are as follows:

- CMMs are not easy to operate. Mostly manufacturing and production experts are those who operate the machine with ease.
- The probe needs to make a physical contact on the surface of the object being measured, so in the process of scanning the probe might damage the surface of the object.
- Though CMMs are very accurate, it takes a lot of time to complete one scanning process. So this could be a bottleneck in industries where the production volume is very high.

1.2.2 Non-contact method

Some of the widely used non-contact measurement techniques are introduced as follows:

1.2.2.1 Laser based techniques

Laser scanning has been used extensively in 3D optical metrology. Following are some of the measurement methods that has different 3D scanning mechanisms:

(1) Triangulation based 3D laser scanner

Triangulation based 3D laser scanning is a non-contact, non-destructive 3D measurement technique. It has a laser probe (emitter) and a detector (receiver) (Franca et al., 2005; Acosta et al., 2006). The laser probe projects a dot or a line of laser light on the object (as represented in Fig. 1.1) and the detector records the reflected laser light signal as it moves over the object. The emitter, receiver and the laser dot or line form a triangle. Therefore, the 3D coordinates are produced via

this triangulation relationship. The main advantage with this system is that it is capable of measuring a large-scale object such as ships or aircraft wings. However, this method is time consuming for real-time measurement since it needs to perform dot-by-dot or line-by-line scanning.

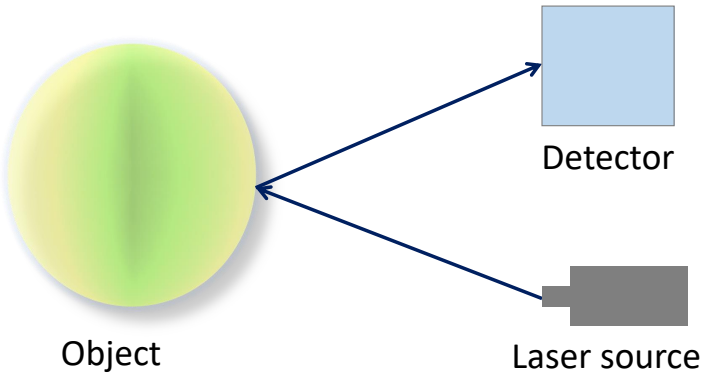

Figure 1.1 A schematic diagram of triangulation based 3D laser scanner.

(2) Time of Flight laser scanner

Time of flight (TOF) laser scanner estimates the surface topography by calculating the time taken for the laser light to reach the laser range detector after striking the object (Lichti and Harvey, 2002). Figure 1.2 is the schematic diagram of a typical time of flight laser scanner. If the time taken for the round trip is t, and the speed of light is c, then the depth is given by $c \cdot t/2$. The main advantage with time of flight is its simplicity in construction and compact design. However, the spatial resolution is limited. Due to the extremely high speed of the light, it is difficult to achieve a high depth resolution (e.g. a timing sensor with a resolution of 3.3 picoseconds is required to resolve 1.00 mm in depth).

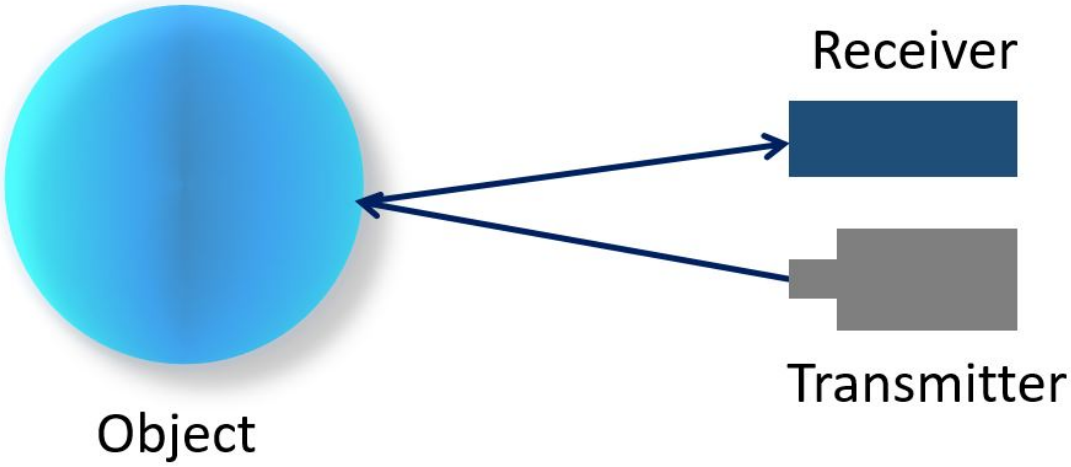

Figure 1.2 A schematic diagram of time of flight laser scanner.

1.2.2.2 Depth from defocus

In this method the depth information of the object is estimated using the level of defocus in different captures. A 3D image can be reconstructed with at least two 2D images captured at two different focus levels (Subbarao and Surya, 1994; Chaudhuri and Rajagopalan, 2012). The object to be scanned is placed on the surface table. Images are captured at different depths. So the points at different locations along the optical axis will have varied amount of blurring. Quantifying the blurring will give the depth information. The main advantage of this method is that the system setup is very simple as only one camera is sufficient for acquiring a 3D image. Also, it can measure steeply sloped surfaces. However, there are a few disadvantages too. If the object being captured doesn't have a rich texture information, then the blurring effect will not be significant and the reconstructed 3D image might not be accurate. Also, it has limited vertical and lateral resolutions (Schechner and Kiryati, 2000).

1.2.2.3 Stereo Vision

Stereo vision system imitates the way in which a human sees the 3D world. A stereo vision system has two cameras (similar to two human eyes as shown in Fig. 1.3) and they capture the same scene from a different view points. The camera has an image plane onto which the 3D real world objects are projected as a 2D image. The relationship between the real world 3D points and their perspective projections on 2D camera image planes is called epipolar geometry. The principle of a typical stereo vision system is illustrated in Fig. 1.4, where O_L and O_R are the centers of projection of the two cameras, E_L and E_R are the epipolar points, and P_L and P_R are the projections of the real world point P on the camera image planes. The projection line $\overline{PO_L}$ and $\overline{PO_R}$ are viewed as a single point P_L and P_R on the left and right camera respectively. Given the projected point P_L on left camera image, by taking advantage of the epipolar geometry, the problem of correspondence finding narrows down from 2D to 1D as the corresponding point captured by the right camera must lie on the line $\overline{E_R P_R}$. Once the correspondence pair is identified, 3D coordinates of a real world point P can be calculated via triangulation.

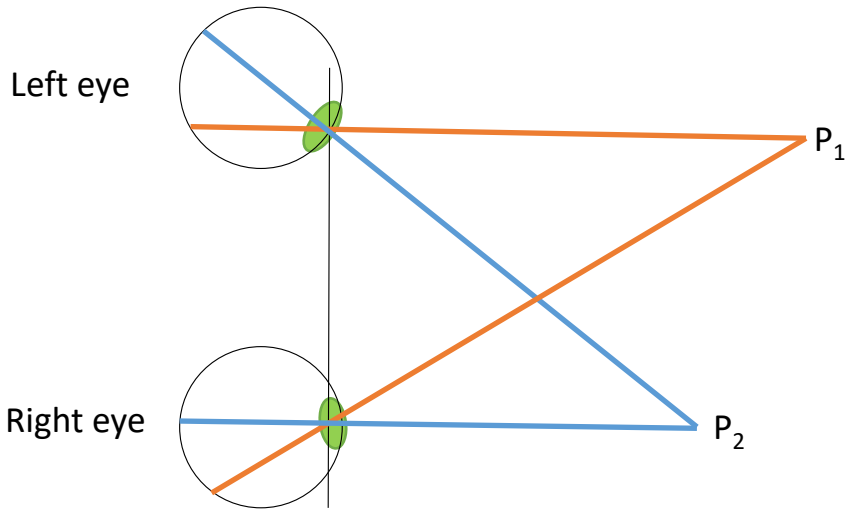

Figure 1.3 Human vision system.

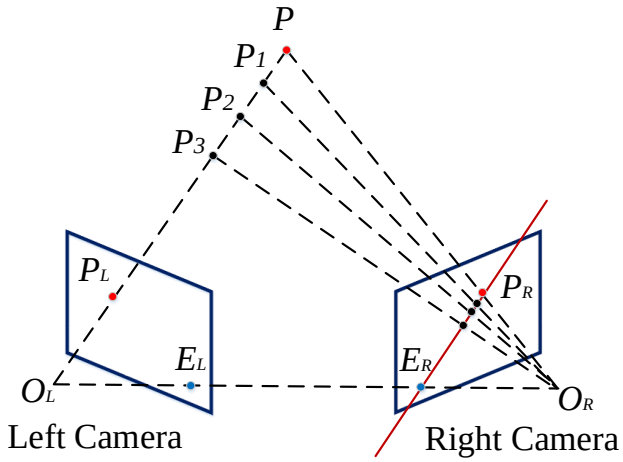

Figure 1.4 Schematic diagram of a stereo vision system.

To perform triangulation, it is important to establish the imaging model of a camera. The projection from a 3D world coordinate to a camera image coordinate is typically described by a pinhole imaging model (Zhang, 2000):

$$s \begin{bmatrix} u \\ v \\ 1 \end{bmatrix} = A \begin{bmatrix} R & t \end{bmatrix} \begin{bmatrix} X \\ Y \\ Z \\ 1 \end{bmatrix}, \tag{1.1}$$

where $[X, Y, Z, 1]^T$ represents the point in the homogeneous world coordinate system, $[u, v, 1]^T$ denotes the point in the homogeneous image coordinate system with the principle point $[u_0, v_0, 1]^T$, and A is the intrinsic matrix represented as

$$A = \begin{bmatrix} f_u & \alpha & u_0 \\ 0 & f_v & v_0 \\ 0 & 0 & 1 \end{bmatrix}. \tag{1.2}$$

Here, f_u and f_v are the focal lengths along u and v axes, respectively. $[R, t]$ is the extrinsic matrix (rotation and translation matrix) that transforms the world coordinate to a camera lens coordinate, and s is the scale factor. There are numerous calibration approaches developed to estimate the extrinsic and intrinsic matrices (Duane, 1971a; Sobel, 1974a; Tsai, 1987a; Zhang, 2000; Lavest et al.,

1998a; Albarelli et al., 2009a; Strobl and Hirzinger, 2011a; Huang et al., 2013c,a). As one can see, the key to successful stereo 3D vision is to correctly establish the correspondence pair. However, stereo vision technique has the problem of finding correspondence pairs in case of a uniform or repetitive texture. An example demonstration of the problem in finding correspondence is clearly depicted in Fig. 1.5. If the left camera captures the image of the checker board and if we try to find the corresponding point (for the one highlighted with the circle) in the right camera's image, the checker board has a repetitive pattern so it is difficult to accurately locate the corresponding point.

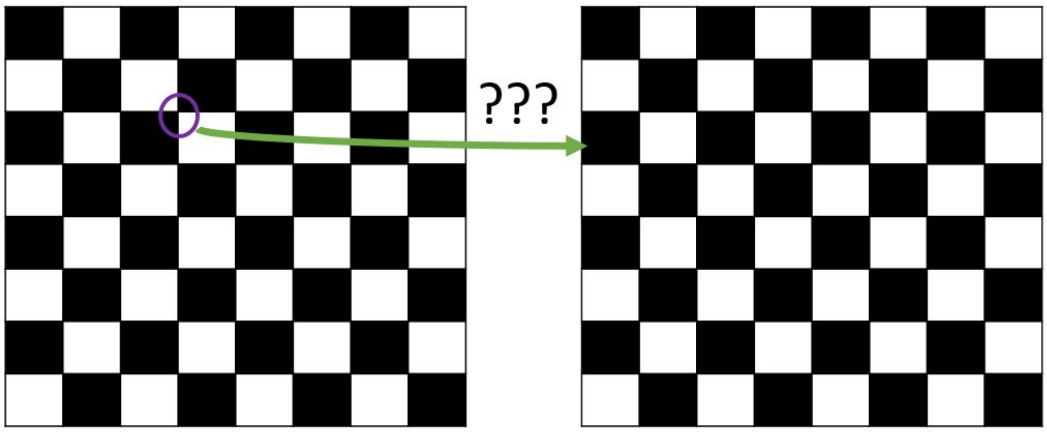

Figure 1.5 Sample object with repetitive texture.

1.2.2.4 Structured Light

The structured light technique is similar to stereo vision but one of the camera is replaced by a projector. This method solves the correspondence problem in stereo vision technique by incorporating an active illumination device. In this method, the projector projects preloaded structured patterns on the object to actively provide features, so it does not need to rely on the texture of the object.

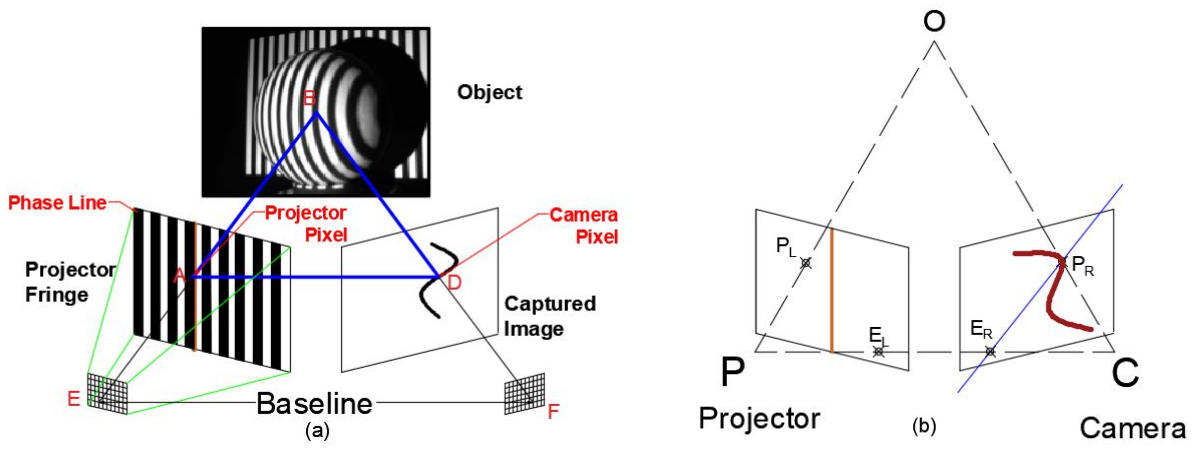

(a) (b)

Figure 1.6 Concept of structured light technique. (a) Schematic diagram explaining the principle of structured light technique; (b) correspondence determination by finding the intersection point between phase line and epipolar line.

Figure 1.6(a) illustrates the principle of the structured light technique. Here **A** represents a projector pixel, **D** represents a camera pixel and the **B** is the object point being imaged. The projector projects preloaded fringe patterns on the object. Since the object usually has curved surfaces, the projected fringe patterns will get distorted by the surface which is then captured by the camera. The determination of the correspondence between camera and projector points with the constraints of epipolar geometry and phase lines is represented in Fig. 1.6(b). For an effective correspondence establishment, many different structured coding strategies were developed over the years. Following are some of the major coding strategies developed for structured light systems:

(1) Random or Pseudo codifications

In this method, patterns that vary in both the directions (u and v) are projected on to the image. Payeur and Desjardins (Payeur and Desjardins, 2009) proposed a color coded random patterns in the form of a square grid. The grid size was 3×3. Each uniquely coded grid makes it easier for the camera to find the correspondence. This random pattern generation can also be done by laser speckles (Huang et al., 2013e). Microsoft Kinect I uses this codification. The main

advantage of this codification is that the entire scene can be coded by a single structured pattern. However, it could be difficult to achieve a high spatial resolution as each unique pattern structure occupies multiple projector pixels.

(2) Binary codifications

As shown in Fig. 1.6, only 1D correspondence is required. Therefore, attempts were also made to create 1D-varying codifications. A straight forward approach is to perform binary codifications. Binary codifications involves projecting a sequence of binary coded patterns (as shown in Fig. 1.7) on to the object being measured. Postdamer and Altschuler (Posdamer and Altschuler, 1982) created a system of encoded arrays in order to establish 1D correspondence. A sequence of black and white patterns are projected on to the object by the projector. Patterns were created with binary numbers 0 and 1 and there were only two intensity levels 0 and 255. Since only 0s and 1s are used it is robust to noise. The correspondence can be found easily from the camera capture as each pixel will have a unique codeword as shown in Fig. 1.8. However, this codification method has a few disadvantages. It is difficult to have a high resolution because the width of the stripe should be more than one pixel size. Besides, to encode a high pixel resolution, the total number of patterns needed can be quite big, which sacrifices the speed of 3D imaging.

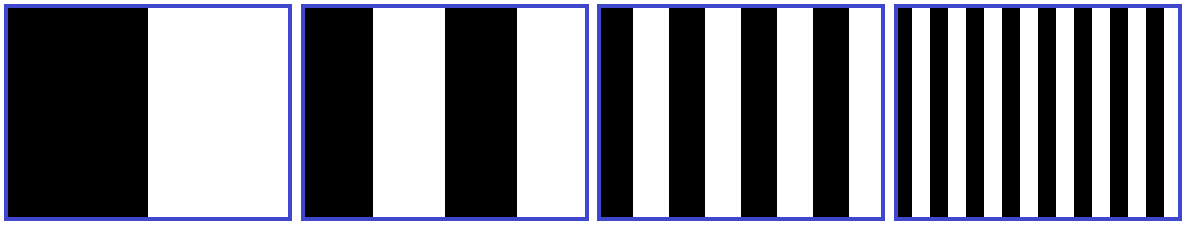

Figure 1.7 Example of codified binary pattern sequence

(3) N-ary codifications

To address the limitations of binary codifications, N-ary codifications was developed to reduce the total number of patterns by using multiple intensity levels between 0 and 255 as shown in Fig. 1.9(a) - 1.9(b). The codeword is different for each pixel and it is determined from the intensity

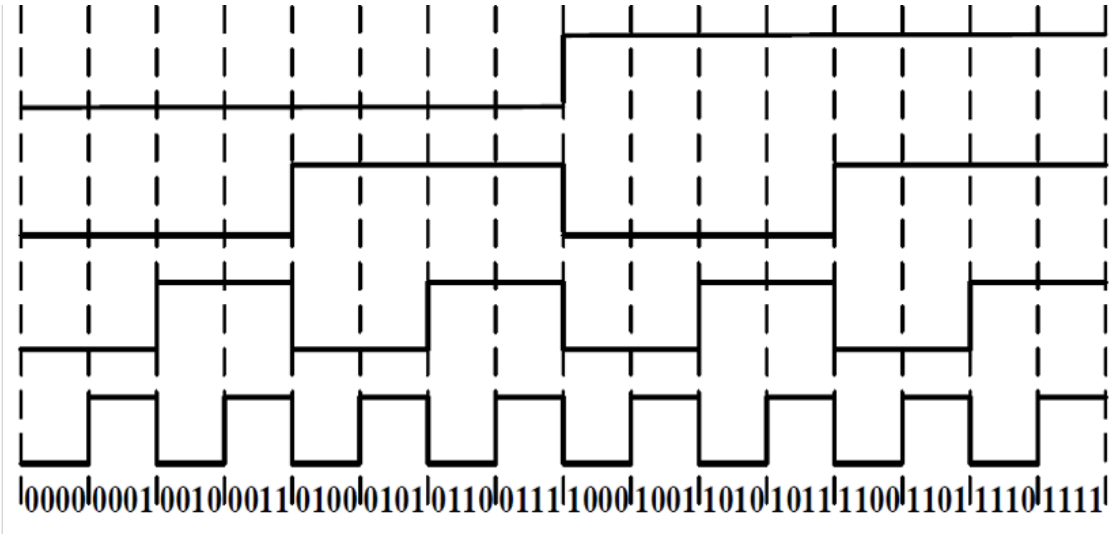

Figure 1.8 An example codifications of binary coded patterns.

ratio. The main advantage of this method is that the number of patterns required for a high resolution capture is significantly less compared to binary codifications and this is because N-ary codifications make use of multiple intensity levels. However, the disadvantage is that the intensity ratio analysis could be sensitive to noise.

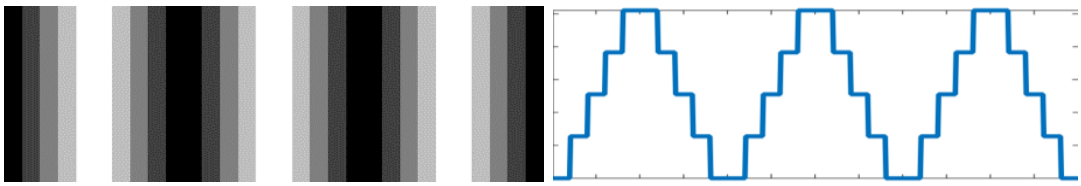

(a) (b)

Figure 1.9 Concept of N-ary codification. (a) An example N-ary pattern; (b) a cross-section of (a) showing multiple gray levels.

1.3 Digital Fringe Projection (DFP)

The binary and N-ary codifications overcome the problem of correspondence pair detection by creating a codeword for each pixel. However, their resolutions are limited since each codeword occupies multiple pixels in width. But, if the binary and N-ary patterns are slightly blurred then they form a sinusoidal pattern. With such sinusoidal patterns it is possible to reach pixel

level resolution because each pixel differs from the neighboring pixel in terms of intensity. Digital fringe projection (DFP) uses sinusoidal patterns for measurement. Computer generated sinusoidal patterns are projected on to the object using a video projector. The sinusoidal patterns get distorted when they fall on the object. The camera captures the distorted patterns from another viewing angle. The DFP technique typically performs carrier phase base analysis since phase information is more robust to noise, ambient light and reflectivity variations. To obtain the phase information, phase shifting method is one of the most commonly used methods (Srinivasan et al., 1984; Huang and Zhang, 2006). Following are the advantages of using phase shifting methods for retrieving phase information:

- As phase shifting methods retrieve information pixel by pixel, it is possible to achieve high spatial resolution.
- High capture speed can be obtained with phase shifting methods as they only require a minimum of three frames for 3D reconstruction.
- It is robust to noise, ambient light and surface variations.

1.4 Objectives

The various codification techniques used for structured light system has been discussed in the previous sections 1.2.2.4 and 1.3. The next step is to use these codified patterns to calibrate the system. The key to accurate 3D shape measurement is the proper calibration of all the elements (projector and camera) of the structured light system. The camera calibration techniques have been well established. On the other hand, the projector calibration is challenging because it cannot capture images. Zhang and Huang (Zhang and Huang, 2006a) developed an enabling technology for calibrating the structured light system, according to which a mirror image was created for the projector by using the horizontal and vertical phase shifted patterns. However, using the orthogonal patterns have few problems too. Grating slits and interferometers cannot produce orthogonal patterns, so they cannot be calibrated by this method. In this research, we aim at

developing a calibration method for the structured light system requiring only unidirectional patterns. There exists one degree-of-freedom (DOF) of redundancy in the conventional Zhang and Huang's calibration method (Zhang and Huang, 2006a), which makes patterns in orthogonal directions over-constrained for system calibration. In this thesis, we will introduce the related theoretical background and the other calibration methods used. Moreover, experimental results will be shown to verify the performance.

1.5 Thesis Organization

This thesis is organized as follows: Chapter 2 introduces the basic principles like fundamentals of sinusoidal signal generation, that is used for 3D shape measurement. Chapter 3 illustrates our calibration framework and Chapter 4 summarizes the whole thesis and discusses some directions for future work.

CHAPTER 2. BASICS OF STRUCTURED LIGHT SYSTEM

In this chapter fundamentals of sinusoidal signal generation that was used in the research will be discussed. Also, the phase-shifting algorithm and other frameworks related to calibration will be explained.

2.1 Fundamentals of sinusoidal signal generation

The idea of sinusoidal signal generation comes from the optical wavefront interference between a reference and a test wavefront. This can be mathematically described (Zhang, 2016) as follows:

$$w_r(x,y) = a_r(x,y)e^{i[\Phi_r(x,y)]} \tag{2.1}$$

$$w_t(x,y) = a_r(x,y)e^{i[\Phi_t(x,y)]} \tag{2.2}$$

$$\Phi(x,y) = \frac{2\pi h(x,y)}{\lambda} \tag{2.3}$$

$$\tag{2.4}$$

where w_r is the reference wavefront and w_t is the test wavefront. The equivalent wavefront when they meet can be described as,

$$w(x,y) = w_r(x,y) + w_t(x,y) \tag{2.5}$$

The intensity of the resultant wavefront (interfering fringe pattern) can be expressed as,

$$I(x,y,t) =\mid w_r(x,y) + w_t(x,y) \mid^2, \tag{2.6}$$

$$I(x,y,t) = I'(x,y) + I''(x,y)\cos[\Phi_t(x,y) - \Phi_r(x,y)], \tag{2.7}$$

$$I'(x,y) = a_r^2(x,y) + a_t^2(x,y), \tag{2.8}$$

$$I''(x,y) = 2a_r(x,y)a_t(x,y) \tag{2.9}$$

where $I'(x,y)$ is the average intensity and $I''(x,y)$ is the intensity modulation. The phase difference can be expressed as,

$$\Phi(x,y) = \Phi_t(x,y) - \Phi_r(x,y) \tag{2.10}$$

Thus the fundamental equation of fringe-analysis can be expressed as,

$$I(x,y) = I'(x,y)) + I''(x,y)\cos[\Phi(x,y)] \tag{2.11}$$

There are three unknowns in Eq. (2.15) $(I'(x,y), I''(x,y), \Phi(x,y))$, so at least three different phase-shifted images are required for extracting the phase $\Phi(x,y)$.

2.1.1 Three-step phase shifting

Many phase shifting algorithms have been developed over the decades. Among them, the three-step phase shifting algorithm requires the minimum number of fringe patterns for extracting the phase. A three-step phase shifting algorithm with equal phase shifts (as illustrated in Fig. 2.1(a)-2.1(c)) is mathematically defined as,

$$I_1(x,y) = I'(x,y) + I''(x,y)\cos[\phi(x,y) - 2\pi/3], \tag{2.12}$$

$$I_2(x,y) = I'(x,y) + I''(x,y)\cos[\phi(x,y)], \tag{2.13}$$

$$I_3(x,y) = I'(x,y) + I''(x,y)\cos[\phi(x,y) + 2\pi/3], \tag{2.14}$$

where $I'(x,y)$ is the average intensity, $I''(x,y)$ represents the intensity modulation, and $\phi(x,y)$ is the phase (as shown in Fig. 2.1(d)) to be solved for. Simultaneously solving the above three equations will lead to,

$$\phi(x,y) = \tan^{-1}\left[\frac{\sqrt{3}(I_1 - I_3)}{2I_2 - I_1 - I_3}\right], \tag{2.15}$$

An arctangent function is used so that the phase value obtained from Eq. (2.15) will range from $-\pi$ to π with a 2π modulus. Spatial or temporal phase unwrapping algorithms could be used to unwrap the phase to obtain a continuous phase map. The unwrapping process essentially locates

the 2π discontinuities and removes the 2π jumps by adding or subtracting $k(x, y)$ multiples of 2π.

$$\Phi(x, y) = \phi(x, y) + k(x, y) \times 2\pi. \tag{2.16}$$

Figure 2.1(e) shows the unwrapped phase map and Fig. 2.1(f) shows the reconstructed 3D geometry.

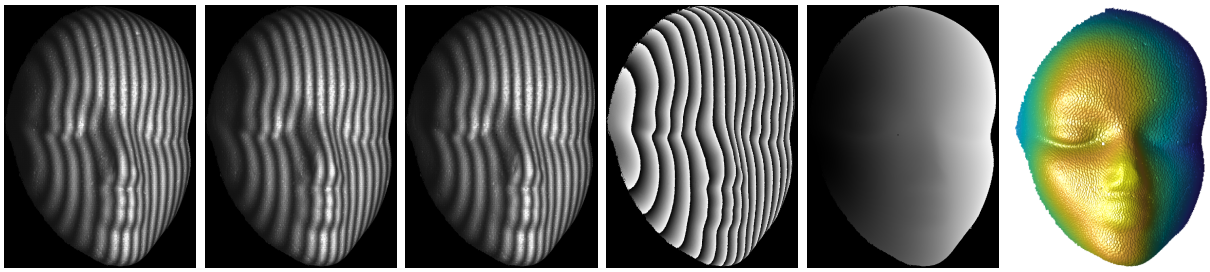

(a) (b) (c) (d) (e) (f)

Figure 2.1 An example procedure for the DFP technique. (a) - (c) Three-step phase shifted patterns; (d) wrapped phase; (e) unwrapped phase; (f) 3D reconstructed geometry.

2.1.2 N-Step phase shifting

If more number of fringe patterns are used then the phase can be retrieved by a least square manner. In a N-step phase shifting algorithm, the intensity of the $k - th$ image with a phase shift of δ_k can be expressed as (Zhang, 2016):

$$I_k(x, y) = I'(x, y) + I''(x, y) \cos[\Phi(x, y) + \delta_k], \tag{2.17}$$

$$\delta_k = \frac{2k\pi}{N} \tag{2.18}$$

The phase after solving the over-constrained N equations by least squares method will be,

$$\Phi(x, y) = \tan^{-1}\left[\frac{\sum_{k=1}^{N} I_k \sin(2k\pi/N)}{\sum_{k=1}^{N} I_k \cos(2k\pi/N)}\right] \tag{2.19}$$

The phase shifting algorithms can extract the phase from the captured fringe images. However, calibration is essential to convert the phase map into 3D geometry. Calibration of the structured light system using orthogonal patterns is explained in section 2.2.

2.2 Calibration using orthogonal patterns

In this section, the well-established popular calibration method proposed by Zhang and Huang (Zhang and Huang, 2006b) will be discussed. In order to perform 3D reconstruction using structured light system, a model should be established for the camera-projector system. Camera and projector share the same optics - pinhole model. The projection for a pin hole model can be defined as,

$$s \begin{pmatrix} u \\ v \\ 1 \end{pmatrix} = A[R|t] \begin{pmatrix} x^w \\ y^w \\ z^w \\ 1 \end{pmatrix} \tag{2.20}$$

where,

s - scaling factor.

A - Intrinsic matrix.

$[R|t]$ - Extrinsic parameters.

(x^w,y^w,z^w) - represent the world coordinate system . The extrinsic matrix is given by,

$$R = \begin{bmatrix} r_{11} & r_{12} & r_{13} \\ r_{21} & r_{22} & r_{23} \\ r_{31} & r_{32} & r_{33} \end{bmatrix}. \tag{2.21}$$

$$t = \begin{bmatrix} t_1 \\ t_2 \\ t_3 \end{bmatrix}. \tag{2.22}$$

The extrinsic parameters transform the points from 3D world coordinate to lens coordinate, they are then transformed to the camera image plane using the intrinsic matrix. The intrinsic matrix is given by,

$$A = \begin{bmatrix} f_u & \gamma & u_o \\ 0 & f_v & v_o \\ 0 & 0 & 1 \end{bmatrix} \tag{2.23}$$

where f_u and f_v represent the effective focal length along the u and v axes, γ represents the skewness of the two axes and (u_0, v_0) represents the principal point. The calibration involves the estimation of the intrinsic and extrinsic parameters to establish a geometric relationship from known points. The camera and projector can be modeled as a pinhole described in Eq. (2.20).

$$s^c \begin{pmatrix} u^c \\ v^c \\ 1 \end{pmatrix} = A^c[R^c|t^c] \begin{pmatrix} x^w \\ y^w \\ z^w \\ 1 \end{pmatrix} \tag{2.24}$$

$$s^p \begin{pmatrix} u^p \\ v^p \\ 1 \end{pmatrix} = A^p[R^p|t^p] \begin{pmatrix} x^w \\ y^w \\ z^w \\ 1 \end{pmatrix} \tag{2.25}$$

The calibration of SLS system involves both the calibration of projector and camera. The camera calibration has been well studied in the past. Initially 3D targets were used for calibration (Duane (1971b)), later a flexible calibration method using 2D targets was developed by Zhang (Zhang (2000)). The camera calibration involves capturing images of the target in different arbitrary poses and then transforming them from the world coordinate to camera coordinate system, but this is not sufficient for a structured light system as the projector also needs to be calibrated. The calibration of the projector is difficult because it does not capture images like the camera. In order to create target images for the projector, a one-to-one mapping has to be established between the camera and projector pixels. The phase value of the codified patterns is used for establishing a relationship between the camera and projector pixels. The phase shifting techniques provide highly accurate phase information. N-step phase shifting (section 2.1.2) is preferred because it has good measurement accuracy. The absolute phase (Eq. 2.26) is obtained by removing the discontinuities using a temporal unwrapping algorithm (which determines the integer $k(x, y)$ times of 2π at discontinuous locations).

$$\Phi(x, y) = \phi(x, y) + k(x, y) \times 2\pi. \tag{2.26}$$

The mapping between the camera and projector pixels can be established using the phase obtained from Eq. 2.26. Consider a pixel (green color in the vertical patterns as shown in Fig. 2.2) in the camera image plane, it also has a corresponding position in the projector's image plane. The pixel's position will change when the patterns move in the horizontal direction, whereas its position will not change when the patterns move in the vertical direction, so each camera pixel corresponds to a line in the projector plane. The shift in the horizontal direction can be uniquely identified by using a set of coded patterns. In this way, the one to many function relating a camera pixel to its corresponding vertical line on the projector plane is expressed as,

$$u^p = f_h(u^c, v^c) \tag{2.27}$$

where f_h represents one to many correspondence function of the point in the camera image plane (u^c, v^c) for the pattern coded in the projector. From the Eq. (2.27), the camera pixel's (u^c, v^c) corresponding vertical line on the projector u^p can be estimated. Similarly for patterns oriented in the horizontal direction, the one to many function relating the camera pixel to its corresponding horizontal line on the projector v^p can be expressed as,

$$v^p = f_v(u^c, v^c) \tag{2.28}$$

Using the Eq. (2.27), (2.28), the corresponding point (u^p, v^p) (on the projector plane) for any camera pixel (u^c, v^c) can be identified.

3D reconstruction is done by solving the camera and projector's projection matrix (Eq. (2.24) and (2.25)). There are 7 unknowns (x^w,y^w,z^w,s^c,s^p,u^p,v^p) but there are only 6 equations. The additional equation is obtained from horizontal or vertical mapping (Eq. (2.27) and (2.28)).

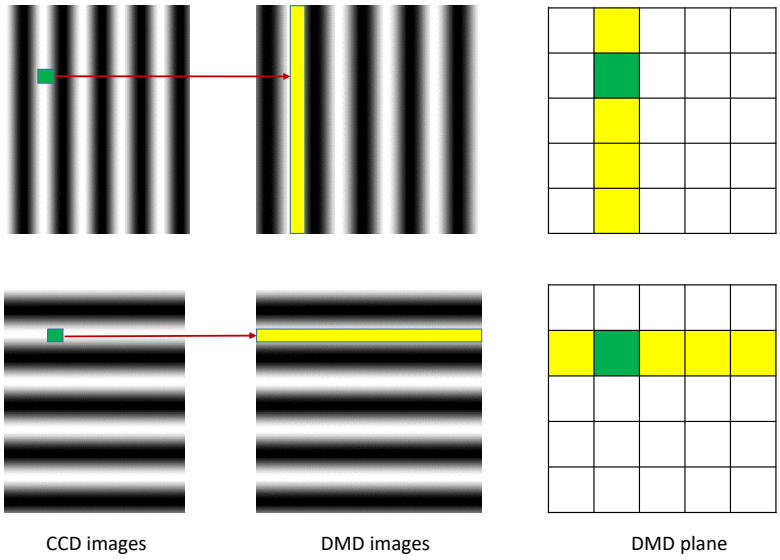

Figure 2.2 Establishment of a one to one mapping between projector and camera pixel using orthogonal patterns.

2.3 Summary

This chapter introduced the basic principles of sinusoidal signal generation. Then the various phase shifting methods used for 3D reconstruction were introduced. Following that, a calibration method using orthogonal patterns was discussed. The next chapter will introduce the proposed calibration method using unidirectional fringe patterns.

CHAPTER 3. CALIBRATION OF STRUCTURED LIGHT SYSTEM USING UNIDIRECTIONAL FRINGE PATTERNS

This chapter will discuss in detail about our calibration framework using unidirectional patterns. This chapter was originally published in *Optics and Lasers in Engineering* (Suresh et al., 2018).

3.1 Introduction

Optical means of three-dimensional (3D) surface measurement has been of great importance in a variety of applications ranging from industrial inspection, robotics, and other applications. Among all optical 3D surface measurement techniques, the structured light technology has been increasingly studied owing to its merits of flexible system setup, high-speed and high-resolution measurements Geng (2011); Gorthi and Rastogi (2010). The measurement accuracy of structured light technology is largely determined by whether one could achieve highly accurate system calibration, which requires accurately calibrating both the image acquisition device (e.g. camera) and the active illumination device (e.g. projector).

The calibration of a camera has been well studied over the past several decades. Initial calibration techniques started from developing techniques with precisely manufactured 3D calibration targets Duane (1971b); Sobel (1974b). Then, Tsai Tsai (1987b) reduced the calibration target to two-dimensional (2D) ones with out-of-plane rigid shift employed to provide depth information. Later, as a milestone in camera calibration, Zhang Zhang (2000) has enabled calibration with 2D targets that can be flexibly arranged with arbitrary orientations. Following Zhang's method, researchers developed advanced technologies that allow the usage of imperfect Lavest et al. (1998b); Albarelli et al. (2009b); Strobl and Hirzinger (2011b); Huang et al. (2013d) or active targets Schmalz et al. (2011); Huang et al. (2013b); Pak (2016). Some recent advances even extended such technology to out-of-focus camera calibration Bell et al. (2016).

For a structured light system, the projector should also be calibrated to realize absolute 3D reconstruction. Yet, such task is comparatively more complicated since unlike a camera, the projector cannot capture images by itself. Methods that extract the exact system parameters (e.g. positions, orientations) of the camera and projector Hu et al. (2003); Mao et al. (2007); Zappa and Busca (2009) provide a solution, yet such methods typically require a time-consuming calibration process. Because of the level of complexity of projector calibration, the reference-plane-based calibration Wen et al. (2010); Xiao et al. (2012); Villa et al. (2012); Xu and Zhang (2012) is still a prevailing technology in the field of optics. Such methods have the merit of a easy-to-compute phase-to-depth conversion. However, this kind of technology requires the reference plane to have a good optical property and surface flatness, and the accuracy of calibration could be affected if the imaging lens is non-telecentric. To address the limitations of a simple reference-plane-based calibration, optimization techniques (e.g. polynomial fitting) Guo et al. (2006); Du and Wang (2007); Merner et al. (2013); Huang et al. (2010); Vo et al. (2012) were used to decode depth information from projector patterns' codifications (e.g. phase value).

Apart from the aforementioned technologies, a different set of technologies were developed which were originated from the concept of treating the projector as an inverse camera Legarda-Sáenz et al. (2004). Zhang and Huang Zhang and Huang (2006a) developed the enabling technology which allows the projector to "capture" images like a camera. The technology essentially maps a camera point to a projector point using absolute phase, in which both horizontal and vertical patterns are required to locate both u and v in 2D projector pixel coordinate. With such mapping scheme, the target images for the projector can also be created and thus the projector can be calibrated using similar strategies as used in camera calibration. Following Zhang and Huang's work, there were a series of different technologies to improve the accuracy including linear interpolation Li et al. (2008), bundle adjustment Yin et al. (2012), residual error compensation Han et al. (2013), or enhanced feature detection Chen et al. (2016). Further innovations have extended the calibration to a system with an out-of-focus projector Li et al. (2014) and to a large-range measurement system An et al. (2016). Such type of methods successfully addressed the long existing puzzle

for projector calibration. However, a crucial limitation of this technology is its requirement of patterns in orthogonal directions. This technology has been proven very efficient for a structured light system with digital fringe projection. Since a video projector is programmable by the user, one can easily generate patterns in orthogonal directions. Yet for other types of systems with different fringe generation schemes (e.g. grating diffractions, interference, etc.), it is challenging to produce patterns in orthogonal directions, making such types of calibration methods difficult to be implemented.

In this research, we introduce a novel calibration method for the structured light system requiring only unidirectional patterns. We mathematically proved that for 3D reconstruction, not all parameters in the projector's projection matrix are required to be known. Therefore, there exists one degree-of-freedom (DOF) of redundancy in the conventional Zhang and Huang's calibration method Zhang and Huang (2006a), which makes patterns in orthogonal directions over-constrained for system calibration. Our method takes one DOF away from projector calibration with an innovated least-square estimation method, where patterns with only one direction are sufficient to support calibration and 3D coordinate computation. Experiments demonstrate that our proposed calibration framework can achieve 3D shape measurement results comparable to the conventional Zhang and Huang's calibration method. Particularly, we achieved an average accuracy of 0.20 mm with a standard deviation of 0.12 mm evaluated by repeatedly measuring a spherical object with $d = 147.726$ mm.

Section 3.2 introduces the related theoretical background as well as our proposed least-square projector partial calibration method. Section 3.3 will demonstrate the experimental results to show the success of our method. Section 3.4 will summarize the contributions of this research.

3.2 Principles

In this section, we first introduce the related theoretical foundations such as the basics of pinhole imaging model, phase shifting technique and camera calibration. Then, we will introduce

our proposed unidirectional projector's least-square partial calibration method and the associated computation of 3D reconstruction.

3.2.1 Pinhole imaging model

In a structured light system, both the camera and fringe projector respect a well-known pinhole imaging model as shown in Fig. 3.1. The associated mathematical formulation is described in Eq. (3.1)

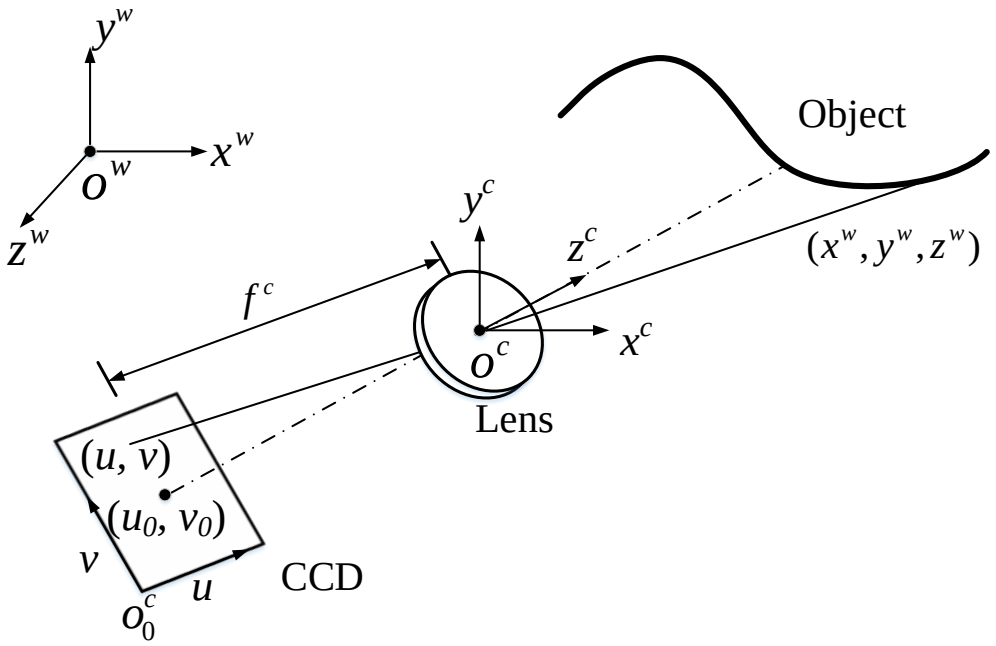

Figure 3.1 Pinhole imaging model. The picture is reprinted from Li et al. (2014)

$$s\begin{bmatrix} u \\ v \\ 1 \end{bmatrix} = \begin{bmatrix} f_u & \gamma & u_0 \\ 0 & f_v & v_0 \\ 0 & 0 & 1 \end{bmatrix} \begin{bmatrix} r_{11} & r_{12} & r_{13} & t_1 \\ r_{21} & r_{22} & r_{23} & t_2 \\ r_{31} & r_{32} & r_{33} & t_3 \end{bmatrix} \begin{bmatrix} x^w \\ y^w \\ z^w \\ 1 \end{bmatrix}. \tag{3.1}$$

In this model, s denotes the scaling factor. r_{ij} and t_i are respectively the rotation and translation parameters which transform a point (x^w, y^w, z^w) in the world coordinate system to a point (x^c, y^c, z^c) in the camera lens coordinate system. f_u, f_v, γ, (u_0, v_0) are all intrinsic parameters of the imaging lens, where f_u, f_v are the effective focal lengths along u and v directions, γ is the

skew factor of u and v axes, and (u_0, v_0) is the principal point on 2D pixel coordinate. To further simplify the model, one can perform matrix multiplication to obtain a combined projection matrix M.

$$\mathbf{M} = \begin{bmatrix} f_u & \gamma & u_0 \\ 0 & f_v & v_0 \\ 0 & 0 & 1 \end{bmatrix} \begin{bmatrix} r_{11} & r_{12} & r_{13} & t_1 \\ r_{21} & r_{22} & r_{23} & t_2 \\ r_{31} & r_{32} & r_{33} & t_3 \end{bmatrix}, \tag{3.2}$$

$$= \begin{bmatrix} m_{11} & m_{12} & m_{13} & m_{14} \\ m_{21} & m_{22} & m_{23} & m_{24} \\ m_{31} & m_{32} & m_{33} & m_{34} \end{bmatrix}, \tag{3.3}$$

The simplified model for the camera and the projector can be expressed using the following equations, where superscript ^{c} and ^{p} denote the camera and the projector, respectively.

$$s^c \begin{bmatrix} u^c \\ v^c \\ 1 \end{bmatrix} = \begin{bmatrix} m^c_{11} & m^c_{12} & m^c_{13} & m^c_{14} \\ m^c_{21} & m^c_{22} & m^c_{23} & m^c_{24} \\ m^c_{31} & m^c_{32} & m^c_{33} & m^c_{34} \end{bmatrix} \begin{bmatrix} x^w \\ y^w \\ z^w \\ 1 \end{bmatrix}, \tag{3.4}$$

$$s^p \begin{bmatrix} u^p \\ v^p \\ 1 \end{bmatrix} = \begin{bmatrix} m^p_{11} & m^p_{12} & m^p_{13} & m^p_{14} \\ m^p_{21} & m^p_{22} & m^p_{23} & m^p_{24} \\ m^p_{31} & m^p_{32} & m^p_{33} & m^p_{34} \end{bmatrix} \begin{bmatrix} x^w \\ y^w \\ z^w \\ 1 \end{bmatrix}, \tag{3.5}$$

3.2.2 Camera calibration and target 3D estimation

The camera calibration has been well established during the past several decades. In this research, we adopted the well-known Zhang's calibration method Zhang (2000) and the camera calibration software toolbox provided by OpenCV. The layout of our calibration target is shown in Fig. 3.2(a), on which the circle centers serve as feature points. Essentially, the camera calibration is composed of two parts: intrinsic and extrinsic calibrations.

The camera intrinsic calibration basically estimates the intrinsic parameters (f_u, f_v, γ, u_0, v_0). We use the camera to take images of different target poses (an example is shown in Fig. 3.2(b)). On each captured target pose, we extract the feature points (e.g. circle centers) for iterative optimization of intrinsic parameters' estimation provided by OpenCV camera calibration toolbox. After intrinsic calibration, we obtained the intrinsic matrix of the camera as

$$\begin{bmatrix} f_u^c & \gamma^c & u_0^c \\ 0 & f_v^c & v_0^c \\ 0 & 0 & 1 \end{bmatrix} = \begin{bmatrix} 2081.481 & 0 & 602.996 \\ 0 & 2087.706 & 533.027 \\ 0 & 0 & 1 \end{bmatrix}. \tag{3.6}$$

In this research, we coincide the world coordinate with the camera lens coordinate (i.e. $x^c = x^w$, $y^c = y^w$, $z^c = z^w$):

$$\begin{bmatrix} r_{11}^c & r_{12}^c & r_{13}^c & t_1^c \\ r_{21}^c & r_{22}^c & r_{23}^c & t_2^c \\ r_{31}^c & r_{32}^c & r_{33}^c & t_3^c \end{bmatrix} = \begin{bmatrix} 1 & 0 & 0 & 0 \\ 0 & 1 & 0 & 0 \\ 0 & 0 & 1 & 0 \end{bmatrix}. \tag{3.7}$$

Then, after matrix multiplication, the final projection matrix is obtained by

$$\begin{bmatrix} m_{11}^c & m_{12}^c & m_{13}^c & m_{14}^c \\ m_{21}^c & m_{22}^c & m_{23}^c & m_{24}^c \\ m_{31}^c & m_{32}^c & m_{33}^c & m_{34}^c \end{bmatrix} = \begin{bmatrix} 2081.481 & 0 & 602.996 & 0 \\ 0 & 2087.706 & 533.027 & 0 \\ 0 & 0 & 1 & 0 \end{bmatrix}. \tag{3.8}$$

The camera extrinsic calibration basically estimates the rotation r_{ij}^{tg} and translation t_i^{tg} parameters from the planar target coordinate $(x^{tg}, y^{tg}, 0)$ to the camera lens coordinate (x^c, y^c, z^c). The definition of the planar target coordinate $(x^{tg}, y^{tg}, 0)$ is shown in Fig. 3.2(a), where the bottom left circle center serves as the principal point. Given that we have already aligned the world coordinate with the camera coordinate, the rotation r_{ij}^{tg} and translation t_i^{tg} parameters will simply transform the planar target points $(x^{tg}, y^{tg}, 0)$ into 3D target points $(x^{wtg}, y^{wtg}, z^{wtg})$ under world coordinate system:

$$\begin{bmatrix} x^{wtg} \\ y^{wtg} \\ z^{wtg} \end{bmatrix} = \begin{bmatrix} r_{11}^{tg} & r_{12}^{tg} & r_{13}^{tg} & t_1^{tg} \\ r_{21}^{tg} & r_{22}^{tg} & r_{23}^{tg} & t_2^{tg} \\ r_{31}^{tg} & r_{32}^{tg} & r_{33}^{tg} & t_3^{tg} \end{bmatrix} \begin{bmatrix} x^{tg} \\ y^{tg} \\ 0 \\ 1 \end{bmatrix} \tag{3.9}$$

The extracted 3D target coordinates are shown in Fig. 3.2(c). Both intrinsic and extrinsic calibration are carried out using OpenCV function *cv::calibrateCamera*.

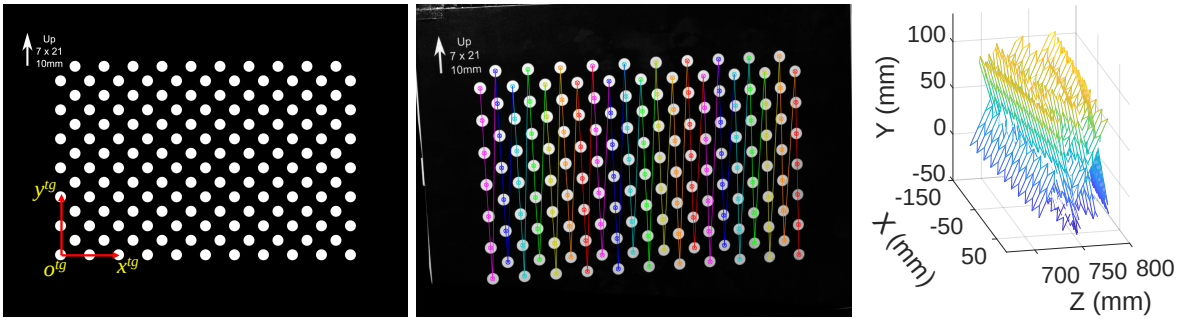

(a) (b) (c)

Figure 3.2 Camera calibration and target 3D estimation. (a) The layout of the calibration target and the definition of target coordinate; (b) the camera image with extracted circle centers; (c) the estimated 3D target orientations.

3.2.3 Least-square phase shifting technique

As aforementioned, it is not easy to create target images for the projector simply because the projector cannot capture images. However, the phase value obtained from pattern codifications can provide extra information to establish the relationship between camera points and projector points. Within different fringe projection techniques, the phase shifting technique Malacara (2007) provides high quality phase extraction with a set of phase shifted fringe images. Some existing techniques include three-step, four-step, least squares and so forth. For a least-square technique with N-steps phase shifting, the i-th fringe image $I^i(x, y)$ can be expressed as

$$I^i(x, y) = I'(x, y) + I''(x, y)\cos(\phi + 2i\pi/N), \tag{3.10}$$

where $I'(x, y)$ represents ambient light or average intensity, $I''(x, y)$ denotes the modulation of intensity, and ϕ is the phase to be extracted. Typically, the more steps (i.e. the bigger N) are used, the better phase quality is going to be obtained. To compute for phase ϕ, one can use the least-square method to solve for the over-constrained simultaneous equations given that $N \geq 3$:

$$\phi(x, y) = -\tan^{-1}\left[\frac{\sum_{i=1}^{N} I^i \sin(2i\pi/N)}{\sum_{i=1}^{N} I^i \cos(2i\pi/N)}\right]. \tag{3.11}$$

Since the computed phase map is in the form of an arctangent function, its value ranges from $-\pi$ to π with 2π discontinuities. To obtain absolute phase map without 2π discontinuities, a temporal phase unwrapping method is typically required which determines the integer number $k(x, y)$ multiples of 2π to be added on the discontinuous points.

$$\Phi(x, y) = \phi(x, y) + k(x, y) \times 2\pi. \tag{3.12}$$

In this research, we adopted a gray intensity coding method Sansoni et al. (1999) for absolute phase retrieval.

3.2.4 Unidirectional least-square projector partial calibration

Once the absolute phase Φ is obtained, assume that Φ varies along v^p direction and starts from 0, one can calculate its corresponding pixel line v^p on the projector image sensor

$$v^p = \Phi \times T/2\pi. \tag{3.13}$$

Here, T is the number of pixels per period of the narrowest fringe patterns used. $T/2\pi$ is simply a scaling factor that converts phase radians into projector pixels. An intuitive visualization of this camera pixel to projector line mapping is shown in Fig. 3.3, in which one can clearly visualize that for any picked camera pixel, its absolute phase value Φ corresponds to a unique pixel line v^p on projector image sensor.

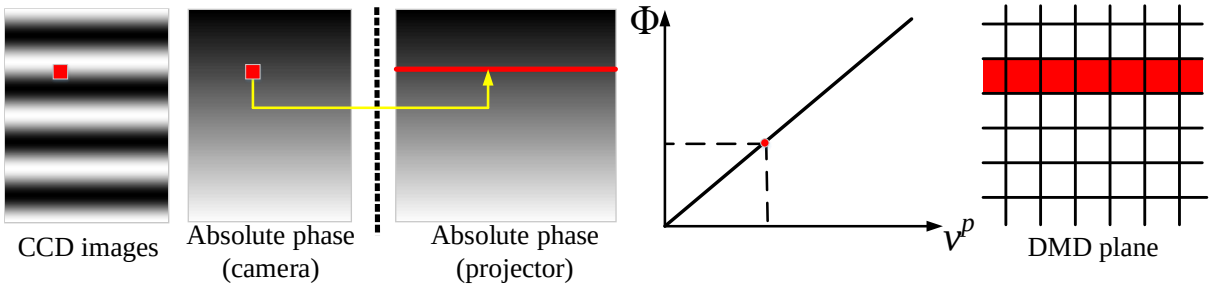

Figure 3.3 Mapping a camera pixel to a projector pixel line using absolute phase. For each picked camera pixel, its computed absolute phase corresponds to a unique line on projector image plane.

In Zhang and Huang's method, both horizontal and vertical absolute phases are required so that a unique mapping point (u^p, v^p) on the projector image sensor is obtained for each target feature point. After mapping each feature point for each target orientation, the same camera calibration procedure is applied to projector calibration, which results in a complete projection matrix being solved for the projector. However, in 3D reconstruction, not all three rows of the projector's projection matrix are required to be known. For instance, by simultaneously solving Eq. (3.4) - Eq. (3.5), a typical 3D reconstruction can be calculated as

$$\begin{bmatrix} x^w & y^w & z^w \end{bmatrix}^T = \mathbf{A}^{-1}\mathbf{b}, \tag{3.14}$$

where

$$\mathbf{A} = \begin{bmatrix} m_{11}^c - u^c m_{31}^c & m_{12}^c - u^c m_{32}^c & m_{13}^c - u^c m_{33}^c \\ m_{21}^c - v^c m_{31}^c & m_{22}^c - v^c m_{32}^c & m_{23}^c - v^c m_{33}^c \\ m_{21}^p - v^p m_{31}^p & m_{22}^p - v^p m_{32}^p & m_{23}^p - v^p m_{33}^p \end{bmatrix} \tag{3.15}$$

$$\mathbf{b} = \begin{bmatrix} u^c m_{34}^c - m_{14}^c & u^c m_{34}^c - m_{24}^c & v^p m_{34}^p - m_{24}^p \end{bmatrix}^T \tag{3.16}$$

As one may notice, if the patterns varying along v^p are used, we do not need to know the first row (m_{1j}^ps) in the projector's projection matrix. This means that there exists one DOF of redundancy in calibration, which provides us possibilities for further simplification.

In reality, from Eq. (3.5), we can obtain another equation of v^p as follows

$$v^p = \frac{s^p v^p}{s^p} = \frac{m_{21}^p x^w + m_{22}^p y^w + m_{23}^p z^w + m_{24}^p}{m_{31}^p x^w + m_{32}^p y^w + m_{33}^p z^w + m_{34}^p}. \tag{3.17}$$

Previously, from camera extrinsic calibration, we have already obtained the 3D coordinates $(x^{wtg}, y^{wtg}, z^{wtg})$ for each calibration target point under world coordinate using Eq. (3.9) (see Fig. 3.2(c)). Given that we also obtained v^p for each target point from absolute phase using Eq. (3.13), if we re-arrange Eq. (3.17) and plug in x^{wtg}, y^{wtg} and z^{wtg} into the equation, we obtain

$$\begin{aligned} \frac{m_{31}^p}{m_{24}^p}(v^p x^{wtg}) + \frac{m_{32}^p}{m_{24}^p}(v^p y^{wtg}) + \frac{m_{33}^p}{m_{24}^p}(v^p z^{wtg}) + \frac{m_{34}^p}{m_{24}^p}(v^p) \\ - \frac{m_{21}^p}{m_{24}^p}(x^{wtg}) - \frac{m_{22}^p}{m_{24}^p}(y^{wtg}) - \frac{m_{23}^p}{m_{24}^p}(z^{wtg}) = 1. \end{aligned} \tag{3.18}$$

After linearizing the equation above, we can reformulate it as

$$\mathbf{Xm} = \mathbf{I}, \tag{3.19}$$

where

$$\mathbf{X} = \begin{bmatrix} v_1^p x_1^{wtg} & v_1^p y_1^{wtg} & v_1^p z_1^{wtg} & v_1^p & -x_1^{wtg} & -y_1^{wtg} & -z_1^{wtg} \\ v_2^p x_2^{wtg} & v_2^p y_2^{wtg} & v_2^p z_2^{wtg} & v_2^p & -x_2^{wtg} & -y_2^{wtg} & -z_2^{wtg} \\ . & . & . & . & . & . & . \\ . & . & . & . & . & . & . \\ . & . & . & . & . & . & . \\ v_n^p x_n^{wtg} & v_n^p y_n^{wtg} & v_n^p z_n^{wtg} & v_n^p & -x_n^{wtg} & -y_n^{wtg} & -z_n^{wtg} \end{bmatrix}, \tag{3.20}$$

$$\mathbf{m} = \begin{bmatrix} \frac{m_{31}^p}{m_{24}^p} & \frac{m_{32}^p}{m_{24}^p} & \frac{m_{33}^p}{m_{24}^p} & \frac{m_{34}^p}{m_{24}^p} & \frac{m_{21}^p}{m_{24}^p} & \frac{m_{22}^p}{m_{24}^p} & \frac{m_{23}^p}{m_{24}^p} \end{bmatrix}^T, \tag{3.21}$$

$$\mathbf{I} = \begin{bmatrix} 1 & 1 & 1 & . & . & . & 1 \end{bmatrix}^T. \tag{3.22}$$

Here, n is the total number of points in all target poses. Since the matrix $\mathbf{X}$ and vector $\mathbf{I}$ are all known, we can solve the unknown vector $\mathbf{m}$ using least-square calculation:

$$\mathbf{m} = \left(\mathbf{X}^T\mathbf{X}\right)^{-1}\mathbf{X}^T\mathbf{I}. \tag{3.23}$$

The result of our $\mathbf{m}$ vector calibration is

$$\mathbf{m} = \begin{bmatrix} -0.048 & -0.504 & 1.958 & -67.416 & -81.450 & -3899.411 & -1014.962 \end{bmatrix}^T \times 10^{-6}. \tag{3.24}$$

3.2.5 3D reconstruction

Once the vector $\mathbf{m}$ is solved, we obtain the parameters m_{ij}/m_{24}, therefore, we can re-formulate the 3D reconstruction as

$$\begin{bmatrix} x^w & y^w & z^w \end{bmatrix}^T = \mathbf{A'}^{-1}\mathbf{b'}, \tag{3.25}$$

where

$$\mathbf{A}' = \begin{bmatrix} m_{11}^c - u^c m_{31}^c & m_{12}^c - u^c m_{32}^c & m_{13}^c - u^c m_{33}^c \\ m_{21}^c - u^c m_{31}^c & m_{22}^c - u^c m_{32}^c & m_{23}^c - u^c m_{33}^c \\ \frac{m_{21}^p}{m_{24}^p} - v^p \frac{m_{31}^p}{m_{24}^p} & \frac{m_{22}^p}{m_{24}^p} - v^p \frac{m_{32}^p}{m_{24}^p} & \frac{m_{23}^p}{m_{24}^p} - v^p \frac{m_{33}^p}{m_{24}^p} \end{bmatrix}, \tag{3.26}$$

$$\mathbf{b}' = \begin{bmatrix} u^c m_{34}^c - m_{14}^c & u^c m_{34}^c - m_{24}^c & v^p \frac{m_{34}^p}{m_{24}^p} - 1 \end{bmatrix}^T. \tag{3.27}$$

From Eq. (3.25) - Eq. (3.27), one can clearly see that the knowledge of the parameters in vector $\mathbf{m}$ is already sufficient. In other words, the projector's partial calibration as introduced above is enough to serve the purpose of 3D reconstruction.

3.3 Experiments

We set up a structured light system as shown in Fig. 3.4 to test our algorithm. We used a digital complementary-metal-oxide-semiconductor CMOS camera (the Imaging Source DFK 33UX174) for image acquisition and a digital-light-processing (DLP) projector (Dell M115HD) for pattern projection. The camera and projector pixel resolutions are set as 1280 $\times$ 1024 and 1280 $\times$ 800, respectively. The camera is attached with a lens of 12 mm focal length (Computar M1214-MP2).

For algorithm validation, we first calibrated the system using both Zhang and Huang's method and our method. While Zhang and Huang's method uses both horizontal and vertical patterns, our method uses horizontal patterns only. For both methods, we used $T = 12$ pixels per period of fringe patterns and $N = 12$ steps phase shifting for both calibration and 3D reconstruction.

In this research, we used a linear model for both the camera and the projector. To demonstrate that the linear model is sufficient in describing our system, we first calibrated the system using both our method and also Zhang and Huang's method, and then take a look at their triangulation error. The triangulation errors are estimated by first triangulating the target points back into world coordinate (x^w, y^w, z^w). The overlay of the triangulated points (x^w, y^w, z^w) and the estimated ideal target points $(x^{wtg}, y^{wtg}, z^{wtg})$ (explained in Eq. (3.9) and Fig. 3.2(c)) are shown in Fig. 3.5(a) -

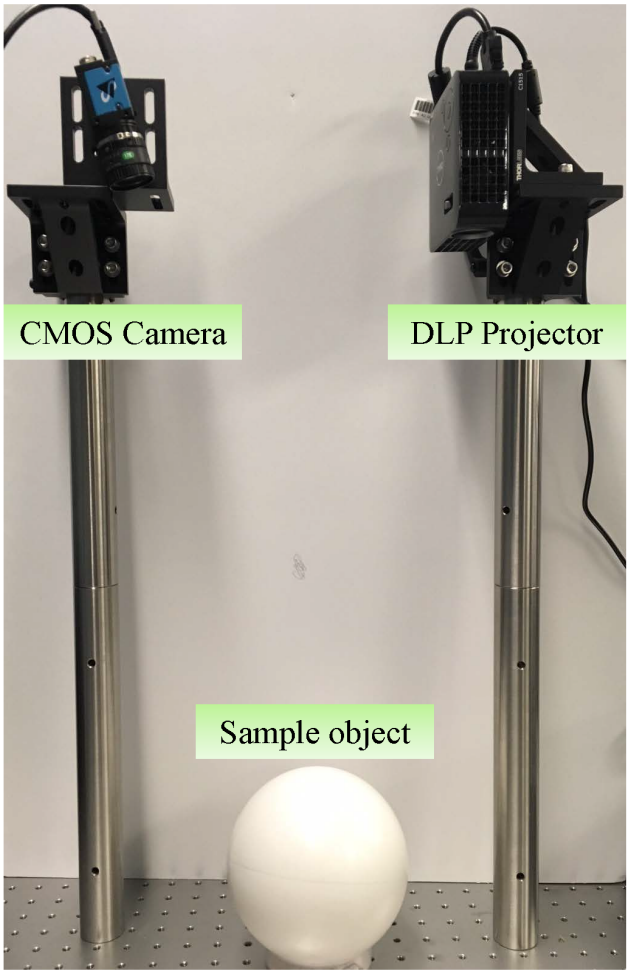

Figure 3.4 A snapshot of the test system.

3.5(b). We then compute the difference as:

$$x^{err}(u,v) = x^{wtg}(u,v) - x^{w}(u,v), \tag{3.28}$$

$$y^{err}(u,v) = y^{wtg}(u,v) - y^{w}(u,v), \tag{3.29}$$

$$z^{err}(u,v) = z^{wtg}(u,v) - z^{w}(u,v). \tag{3.30}$$

The triangulation errors of both our method and also Zhang and Huang's method are shown in Fig. 3.5(c) - 3.5(d). The root-mean-square (RMS) errors for X, Y and Z are 0.06 mm, 0.06 mm and 0.19 mm for our method; and 0.06 mm, 0.05 mm and 0.18 mm for Zhang and Huang's method. As one may see, our method produces the same level of triangulation error compared to Zhang and

Huang's method. Consider the overall depth volume of calibration [i.e. 200 mm (X) $\times$ 150 mm (Y) $\times$ 120 mm (Z)], the triangulation error is less than 0.1%. Overall, the Z error is larger than X and Y because of the varying focus convergence across the depth volume. Other possible error sources include the estimation of circle centers and the planarity level of the calibration target.

Table 3.1 Measurement results of a sphere after repeated testing

Proposed method			Zhang and Huang's method		
Test No.	Mean error (mm)	Std error (mm)	Test No.	Mean error (mm)	Std error (mm)
1	0.18	0.11	1	0.46	0.13
2	0.10	0.13	2	0.33	0.14
3	0.15	0.15	3	0.38	0.16
4	0.32	0.12	4	0.56	0.14
5	0.16	0.10	5	0.04	0.10
6	0.26	0.13	6	0.44	0.15
7	0.02	0.13	7	0.23	0.13
8	0.23	0.11	8	0.03	0.10
9	0.29	0.13	9	0.47	0.14
10	0.29	0.12	10	0.45	0.13

We measured a big white plastic spherical object to test the accuracy of our algorithm. We first measured the diameter of the sphere using a 5 - 6 inch range precision mechanical outside micrometer (Model: Starrett 436.1). The measured diameter is 5.816 $\pm$ 0.001 in, or equivalently, 147.726 $\pm$ 0.003 mm. To show that our calibration method indeed reconstructs absolute 3D geometry, we measured the sphere using both our proposed calibration method and also the Zhang and Huang's calibration method. To evaluate the accuracy of both calibration methods, we compared the reconstructed 3D geometries with an ideal sphere of the same size (i.e. d = 147.726 mm). Figure 3.6(a) and 3.6(d) respectively demonstrate the overlay of the reconstructed 3D geometries with an ideal sphere with a 147.726 mm diameter. The corresponding error maps are shown in Fig. 3.6(b) and 3.6(e). To better visualize the error maps, we selected the same cross section corresponding to the peak point and plotted them in Fig. 3.6(c) and 3.6(f). The mean error and standard deviation are 0.10 mm and 0.13 mm for our method; and 0.33 mm and 0.14 mm for Zhang and Huang's method. To test the measurement stability, we measured the sphere 10 times

at different spatial locations and the results are listed in Table 3.1. The results indicate that our method produces the same level but with a slightly higher accuracy compared to the Zhang and Huang's method. We believe the major reason is because of the sensitivity bias in a well-designed system. Figure 3.7 demonstrates this phenomenon of sensitivity bias. Figure 3.7(a) shows that the pattern has the best sensitivity (i.e. apparent pattern distortion by object curvature) in one (i.e. horizontal) pattern direction; yet Fig. 3.7(b) shows that there is almost zero sensitivity (i.e. no distortion by object curvature) in the orthogonal (i.e. vertical) pattern direction. Our previous finding Li and Zhang (2014) showed that under such a well-designed system, if both horizontal and vertical patterns are used for calibration (same as Zhang and Huang's method), the measurement accuracy of a geometric shape with curvature could be jeopardized. Yet, our method only uses horizontal patterns which has the highest sensitivity under such system setup. Therefore, the problem associated with sensitivity bias can be circumvented. This experiment clearly demonstrates the success of our method.

To further evaluate the accuracy, we take an additional set of 6 target poses within our calibration volume and measured the lengths of two line segments $\overline{AB}$ and $\overline{CD}$ as shown in Fig. 3.8. The line segments are formed by four circle centers and the lengths of the two line segments are $12 \times 10\sqrt{2} = 169.70$ mm. Table 3.2 shows the measured lengths of the line segments using both our method and Zhang and Huang's method. The results show that our method can produce results at the same error level compared to Zhang and Huang's method. The mean and RMS errors are 0.26 mm and 0.34 mm for our method, and 0.24 mm and 0.31 mm for Zhang and Huang's method. The results further validate the success of our calibration method.

3.4 Summary

We developed a novel unidirectional calibration framework for structured light system. By removing one DOF of redundancy in conventional structured light system calibration, our method does not require the projection of fringe patterns in orthogonal directions, and thus could be potentially applicable to unidirectional fringe projection systems. Experiments demonstrate that our

Table 3.2 Measurement result of two diagonals on calibration board using proposed method and Zhang and Huang's method.

Proposed method				
Pose No.	$\overline{AB}$ (mm)	Error (mm)	$\overline{CD}$ (mm)	Error (mm)
Pose 1	169.74	0.04	169.83	0.13
Pose 2	169.46	-0.24	169.82	0.12
Pose 3	169.72	0.02	169.74	0.04
Pose 4	169.44	-0.26	169.66	-0.04
Pose 5	169.76	0.06	170.58	0.88
Pose 6	169.89	0.19	170.13	0.43
Mean	169.67	-0.03	169.96	0.26
Std	0.18	NA	0.34	NA
Zhang and Huang's method				
Pose No.	$\overline{AB}$ (mm)	Error (mm)	$\overline{CD}$ (mm)	Error (mm)
Pose 1	169.63	-0.07	169.78	0.08
Pose 2	169.46	-0.24	169.85	0.15
Pose 3	169.61	-0.08	169.72	0.01
Pose 4	169.51	-0.18	169.75	0.05
Pose 5	169.64	-0.05	170.54	0.84
Pose 6	169.78	0.08	170.04	0.33
Mean	169.60	-0.10	169.94	0.24
Std	0.12	NA	0.31	NA

calibration method can achieve 3D shape measurement with an accuracy comparable to conventional orthogonal calibration method within a measurement range of 200 mm (X) $\times$ 150 mm (Y) $\times$ 120 mm (Z). Specifically, we achieved an average accuracy of 0.20 mm with a standard deviation of 0.12 mm by repeatedly measuring a spherical object with $d = 147.726$ mm. The same technology should be adaptable to any other pattern directions given that a simple rotation can be applied to transform the image coordinate system Li and Zhang (2014).

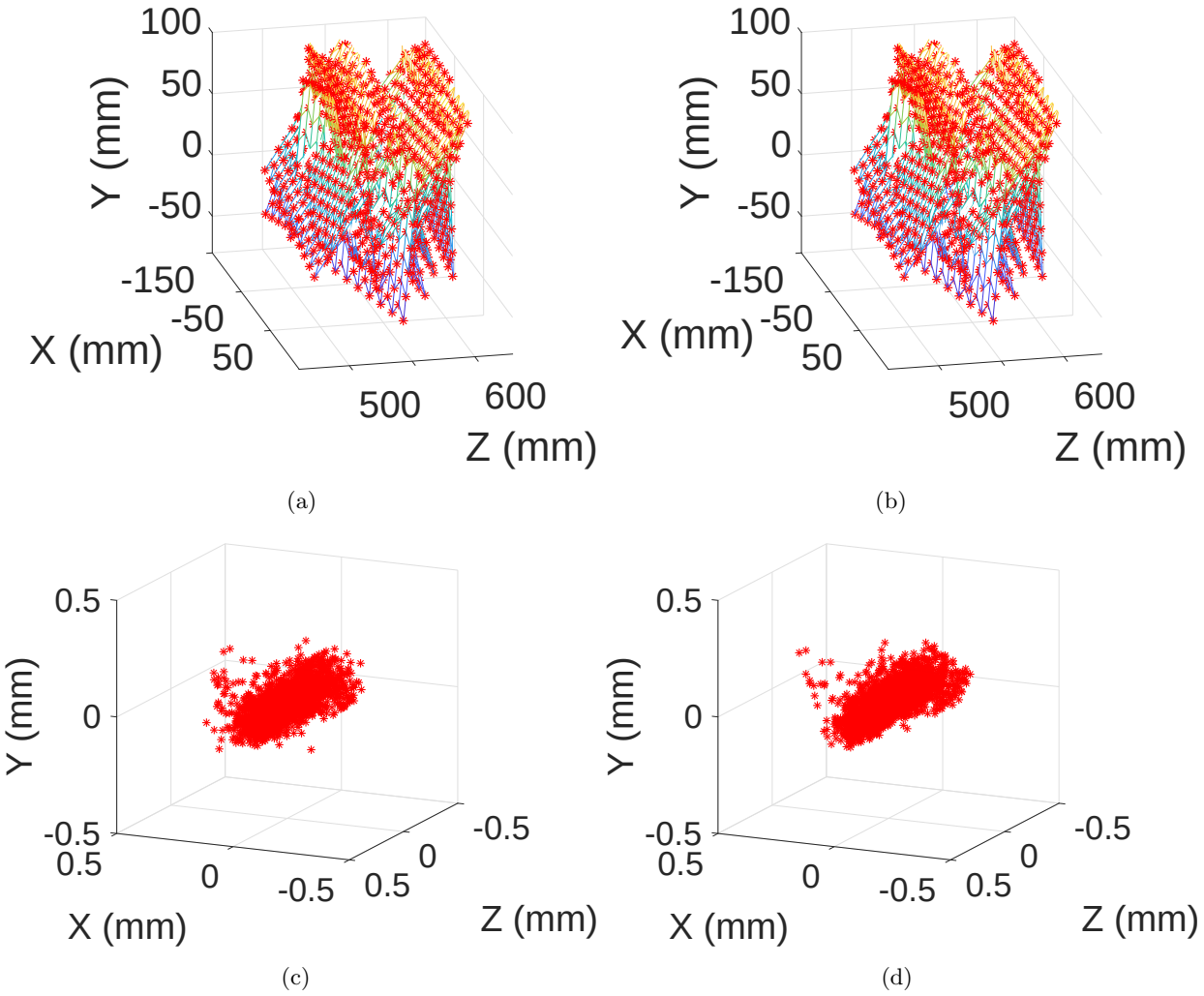

Figure 3.5 Evaluation of triangulation error. (a) Overlay of the triangulated points (x^w, y^w, z^w) and the estimated ideal target points $(x^{wtg}, y^{wtg}, z^{wtg})$ using our method; (b) overlay of the triangulated points (x^w, y^w, z^w) and the estimated ideal target points $(x^{wtg}, y^{wtg}, z^{wtg})$ using Zhang and Huang's method; (c) error from our method, the RMS errors for X, Y and Z are 0.06 mm, 0.06 mm and 0.19 mm; (b) error from Zhang and Huang's method, The RMS errors for X, Y and Z are 0.06 mm, 0.05 mm and 0.18 mm.

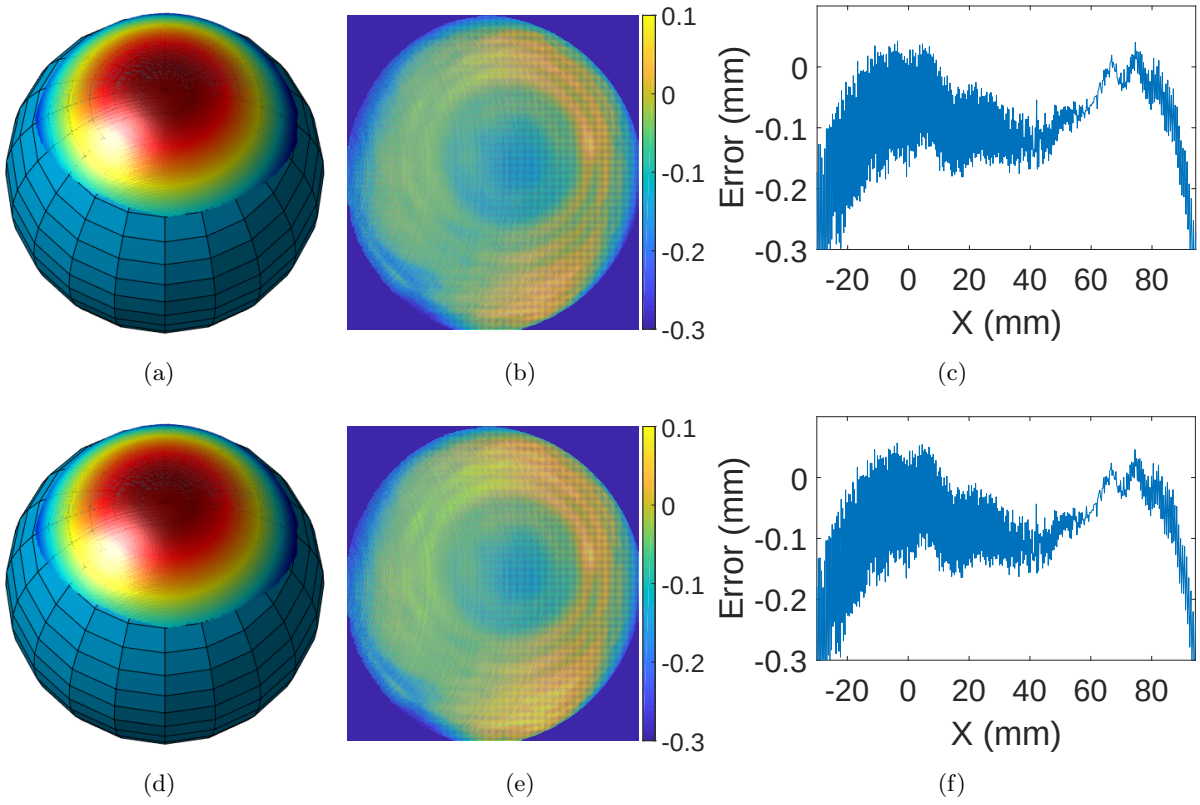

Figure 3.6 A sample evaluation of the measurement accuracies. (a) Overlay of the measured sphere using proposed method and the large ideal sphere with a 147.726 mm diameter; (b) error maps of (a) (mean error: 0.10 mm; standard deviations: 0.13 mm); (c) a cross section of (b); (d) - (f) corresponding results obtained using conventional Zhang and Huang's method (mean error: 0.33 mm; standard deviations: 0.14 mm).

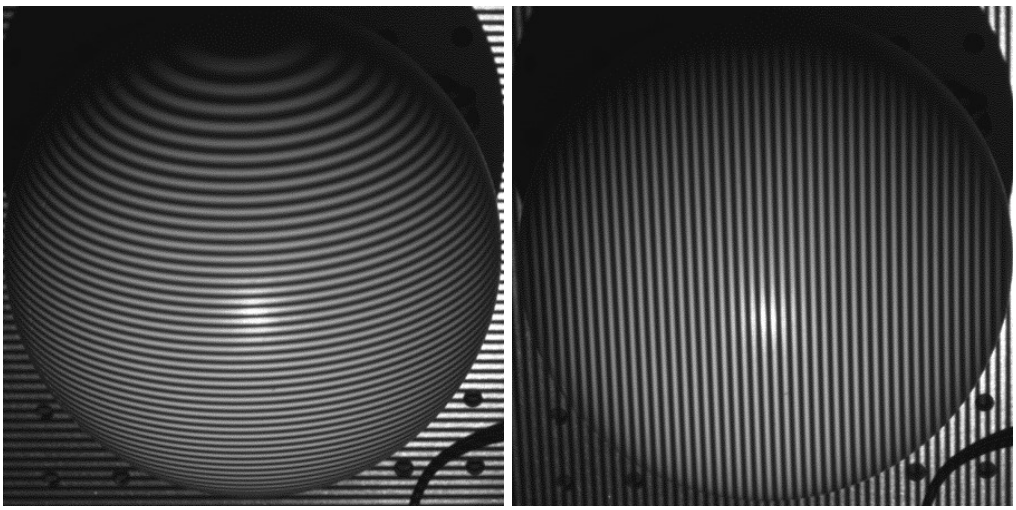

(a) (b)

Figure 3.7 Illustrations of sensitivity bias in a well-designed system. (a) A sample fringe image with horizontal pattern projection (high sensitivity, apparent pattern distortion by geometry); (b) a sample fringe image with vertical pattern projection (almost no sensitivity or pattern distortion by geometry).

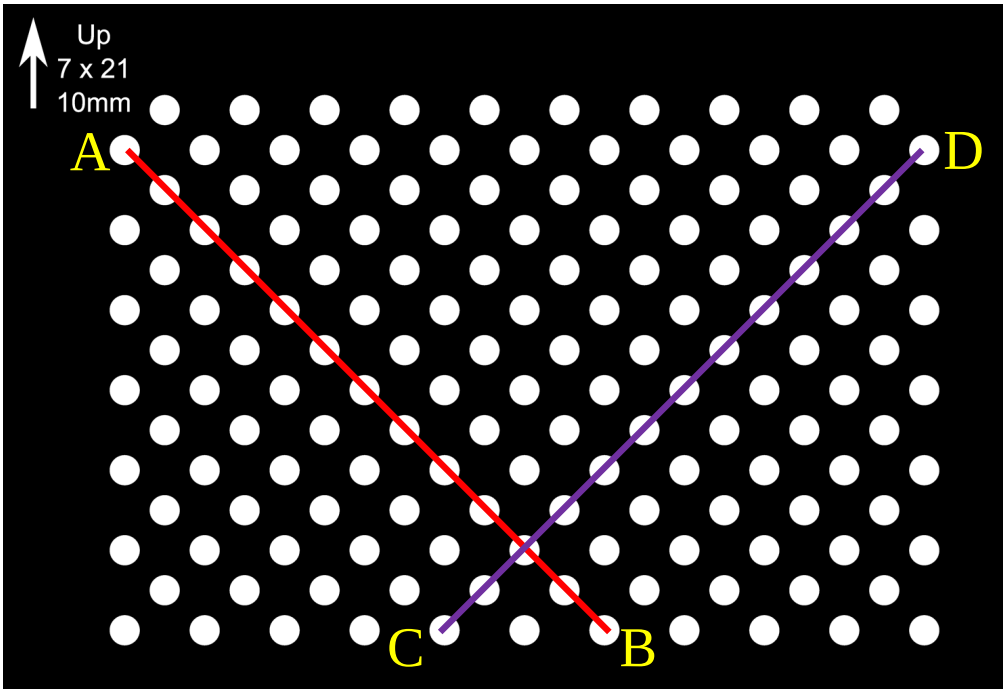

Figure 3.8 Illustration of measured two line segments $\overline{AB}$ and $\overline{CD}$ on our calibration target.

CHAPTER 4. SUMMARY AND FUTURE SCOPE OF WORK

This chapter summarizes the contributions of the research work and proposes some future scope of work.

4.1 Research Achievements

In this research, we presented a new calibration technique for the structured light system with the fringe pattern in only one direction. We theoretically proved that there is a degree of freedom of redundancy in the conventional calibration method using orthogonal fringe patterns. Thus by removing the redundancy in the conventional calibration method, it becomes possible to calibrate the system using unidirectional patterns. Experiments were conducted with a spherical ball to verify the effectiveness of the proposed calibration method. From the results, it has been evident that our calibration method can achieve 3D shape measurement with an accuracy comparable to conventional orthogonal calibration method within a measurement range of 200 mm $\times$ 150 mm $\times$ 120 mm (X,Y and Z respectively). Specifically, we achieved an average accuracy of 0.20 mm with a standard deviation of 0.12 mm by repeatedly measuring a spherical object. In this way, the time involved for calibration can be reduced. This calibration approach can be applied to systems which can produce patterns only in one direction.

4.2 Future Work

The proposed calibration method can be used for calibrating other systems. Following are some of the potential applications:

- *Flexible calibration for diffraction grating.* As discussed in section 3.1, it is difficult to calibrate diffraction grating (as shown in Fig. 4.1) using orthogonal patterns as the slits (as illustrated in Fig. 4.2) used for splitting the incoming light can produce patterns only in one

direction based on the opening in it. A flexible calibration system can be made for such systems using unidirectional patterns.

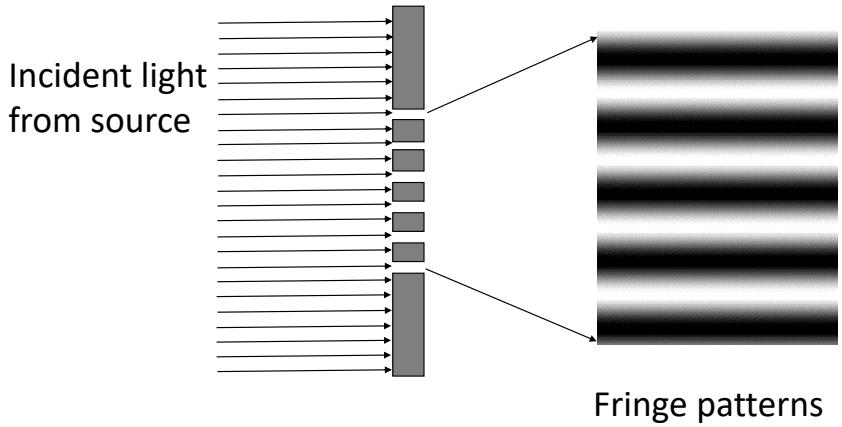

Figure 4.1 Schematic diagram of a diffraction grating

- *Calibration of optical interferometers.* Interferometers produce patterns when two coherent light sources S_1 and S_2 (as depicted in Fig. 4.3) of the same frequency interfere with each other. Like the diffraction gratings, optical interferometers cannot produce orthogonal patterns. A calibration technique for interferometers using unidirectional patterns can be developed.

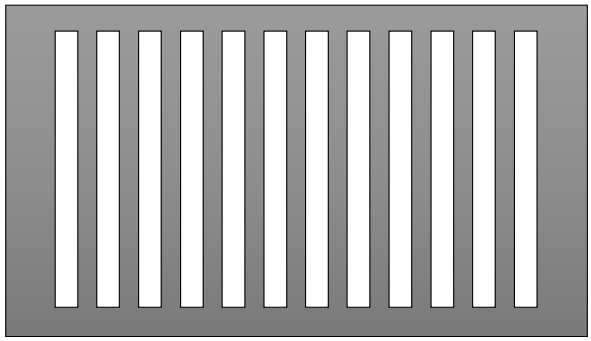

Figure 4.2 Grating slit

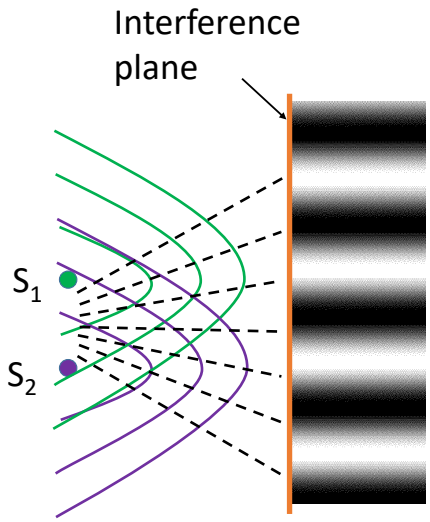

Figure 4.3 Schematic of wavefront interference

BIBLIOGRAPHY

Acosta, D., García, O., and Aponte, J. (2006). Laser triangulation for shape acquisition in a 3d scanner plus scan. In *Electronics, Robotics and Automotive Mechanics Conference, 2006*, volume 2, pages 14–19. IEEE.

Albarelli, A., Rodolà, E., and Torsello, A. (2009a). Robust camera calibration using inaccurate targets. *Trans. Pattern Anal. Mach. Intell*, 31(2):376–383.

Albarelli, A., Rodolà, E., and Torsello, A. (2009b). Robust camera calibration using inaccurate targets. *Trans. Pattern Anal. Mach. Intell.*, 31(2):376–383.

An, Y., Bell, T., Li, B., Xu, J., and Zhang, S. (2016). Method for large-range structured light system calibration. *Appl. Opt.*, 55(33):9563–9572.

Bailey, R.-P. S. (2010). Coordinate measuring machine. US Patent 7,793,425.

Bell, T., Xu, J., and Zhang, S. (2016). Method for out-of-focus camera calibration. *Applied optics*, 55(9):2346–2352.

Bhatia, G., Vannier, M. W., Smith, K. E., Commean, P. K., Riolo, J., and Young, V. L. (1994). Quantification of facial surface change using a structured light scanner. *Plastic and reconstructive surgery*, 94(6):768–774.

Chaudhuri, S. and Rajagopalan, A. N. (2012). *Depth from defocus: a real aperture imaging approach*. Springer Science & Business Media.

Chen, R., Xu, J., Chen, H., Su, J., Zhang, Z., and Chen, K. (2016). Accurate calibration method for camera and projector in fringe patterns measurement system. *Appl. Opt.*, 55(16):4293–4300.

Devi, M. A., Ravi, S., Vaishnavi, J., and Punitha, S. (2016). Classification of cervical cancer using artificial neural networks. *Procedia Computer Science*, 89:465–472.

Dhond, U. R. and Aggarwal, J. K. (1989). Structure from stereo-a review. *IEEE transactions on systems, man, and cybernetics*, 19(6):1489–1510.

Du, H. and Wang, Z. (2007). Three-dimensional shape measurement with an arbitrarily arranged fringe projection profilometry system. *Opt. Lett.*, 32(16):2438–2440.

Duane, C. B. (1971a). Close-range camera calibration. *Photogrammetric Eng.*, 37(8):855–866.

Duane, C. B. (1971b). Close-range camera calibration. *Photogrammetric Eng.*, 37(8):855–866.

Franca, J. G. D., Gazziro, M. A., Ide, A. N., and Saito, J. H. (2005). A 3d scanning system based on laser triangulation and variable field of view. In *Image Processing, 2005. ICIP 2005. IEEE International Conference on*, volume 1, pages I–425. IEEE.

Geng, J. (2011). Structured-light 3d surface imaging: a tutorial. *Advances in Opt. and Photonics*, 3(2):128–160.

Gorthi, S. and Rastogi, P. (2010). Fringe projection techniques: Whither we are? *Opt. Laser. Eng.*, 48:133–140.

Guo, H., Chen, M., and Zheng, P. (2006). Least-squares fitting of carrier phase distribution by using a rational function in fringe projection profilometry. *Opt. Lett.*, 31(24):3588–3590.

Han, D., Chimienti, A., and Menga, G. (2013). Improving calibration accuracy of structured light systems using plane-based residual error compensation. *Opt. Eng.*, 52(10):104106–104106.

Hu, Q., Huang, P. S., Fu, Q., and Chiang, F.-P. (2003). Calibration of a three-dimensional shape measurement system. *Opt. Eng.*, 42(2):487–493.

Huang, L., Chua, P. S., and Asundi, A. (2010). Least-squares calibration method for fringe projection profilometry considering camera lens distortion. *Appl. Opt.*, 49(9):1539–1548.

Huang, L., Zhang, Q., and Asundi, A. (2013a). Camera calibration with active phase target: improvement on feature detection and optimization. *Opt. Lett.*, 38(9):1446–1448.

Huang, L., Zhang, Q., and Asundi, A. (2013b). Camera calibration with active phase target: improvement on feature detection and optimization. *Opt. Lett.*, 38(9):1446–1448.

Huang, L., Zhang, Q., and Asundi, A. (2013c). Flexible camera calibration using not-measured imperfect target. *Appl. Opt.*, 52(25):6278–6286.

Huang, L., Zhang, Q., and Asundi, A. (2013d). Flexible camera calibration using not-measured imperfect target. *Appl. Opt.*, 52(25):6278–6286.

Huang, P. S. and Zhang, S. (2006). Fast three-step phase-shifting algorithm. *Applied optics*, 45(21):5086–5091.

Huang, Y., Shang, Y., Liu, Y., and Bao, H. (2013e). Handbook of 3d machine vision: Optical metrology and imaging, chap. 3d shapes from speckle. *CRC*, pages 33–56.

Iyengar, A. K., Sugimoto, H., Smith, D. B., and Sacks, M. S. (2001). Dynamic in vitro quantification of bioprosthetic heart valve leaflet motion using structured light projection. *Annals of biomedical engineering*, 29(11):963–973.

Laughner, J. I., Zhang, S., Li, H., Shao, C. C., and Efimov, I. R. (2012). Mapping cardiac surface mechanics with structured light imaging. *American Journal of Physiology-Heart and Circulatory Physiology*, 303(6):H712–H720.

Lavest, J., Viala, M., and Dhome, M. (1998a). Do we really need an accurate calibration pattern to achieve a reliable camera calibration? In *European Conference on Computer Vision*, pages 158–174.

Lavest, J., Viala, M., and Dhome, M. (1998b). Do we really need an accurate calibration pattern to achieve a reliable camera calibration? In *Proc. ECCV*, pages 158–174. Springer.

Legarda-Sáenz, R., Bothe, T., and Jüptner, W. P. (2004). Accurate procedure for the calibration of a structured light system. *Opt. Eng.*, 43(2):464–471.

Li, B., Karpinsky, N., and Zhang, S. (2014). Novel calibration method for structured light system with an out-of-focus projector. *Appl. Opt.*, 53(16):3415–3426.

Li, B. and Zhang, S. (2014). Structured light system calibration method with optimal fringe angle. *Appl. Opt.*, 53(33):7942–7950.

Li, Z., Shi, Y., Wang, C., and Wang, Y. (2008). Accurate calibration method for a structured light system. *Opt. Eng.*, 47(5):053604–053604.

Lichti, D. D. and Harvey, B. (2002). The effects of reflecting surface material properties on time-of-flight laser scanner measurements. *tc*, 2:1.

Malacara, D., editor (2007). *Optical Shop Testing*. John Wiley and Sons, New York, NY, 3rd edition.

Mao, X., Chen, W., and Su, X. (2007). Improved fourier-transform profilometry. *Appl. Opt.*, 46(5):664–668.

May, J. D. and Gosselin, C. E. (1986). Probe for coordinate measuring machine. US Patent 4,612,622.

Mehta, R. P., Zhang, S., and Hadlock, T. A. (2008). Novel 3-d video for quantification of facial movement. *Otolaryngology—Head and Neck Surgery*, 138(4):468–472.

Merner, L., Wang, Y., and Zhang, S. (2013). Accurate calibration for 3d shape measurement system using a binary defocusing technique. *Opt. Laser Eng.*, 51(5):514–519.

Pak, A. (2016). The concept of smooth generic camera calibration for optical metrology. *tm-Technisches Messen*, 83(1):25–35.

Payeur, P. and Desjardins, D. (2009). Structured light stereoscopic imaging with dynamic pseudo-random patterns. In *International Conference Image Analysis and Recognition*, pages 687–696. Springer.

Pettersson, B. (2009). Coordinate measuring machine. US Patent 7,591,077.

Posdamer, J. L. and Altschuler, M. (1982). Surface measurement by space-encoded projected beam systems. *Computer graphics and image processing*, 18(1):1–17.

Sansoni, G., Carocci, M., and Rodella, R. (1999). Three-dimensional vision based on a combination of gray-code and phase-shift light projection: Analysis and compensation of the systematic errors. *Appl. Opt.*, 38:6565–6573.

Schechner, Y. Y. and Kiryati, N. (2000). Depth from defocus vs. stereo: How different really are they? *International Journal of Computer Vision*, 39(2):141–162.

Schmalz, C., Forster, F., and Angelopoulou, E. (2011). Camera calibration: active versus passive targets. *Opt. Eng.*, 50(11):113601–113601.

Sobel, I. (1974a). On calibrating computer controlled cameras for perceiving 3-d scenes. *Artificial Intelligence*, 5(2):185–198.

Sobel, I. (1974b). On calibrating computer controlled cameras for perceiving 3-d scenes. *Artificial Intelligence*, 5(2):185–198.

Srinivasan, V., Liu, H.-C., and Halioua, M. (1984). Automated phase-measuring profilometry of 3-d diffuse objects. *Applied optics*, 23(18):3105–3108.

Strobl, K. H. and Hirzinger, G. (2011a). More accurate pinhole camera calibration with imperfect planar target. In *IEEE International Conference on Computer Vision Workshops (ICCV Workshops),*, pages 1068–1075.

Strobl, K. H. and Hirzinger, G. (2011b). More accurate pinhole camera calibration with imperfect planar target. In *IEEE International Conference on Computer Vision*, pages 1068–1075. IEEE.

Subbarao, M. and Surya, G. (1994). Depth from defocus: a spatial domain approach. *International Journal of Computer Vision*, 13(3):271–294.

Suresh, V., Holton, J., and Li, B. (2018). Structured light system calibration with unidirectional fringe patterns. *Optics and Lasers in Engineering*, 106:86–93.

Tsai, R. (1987a). A versatile camera calibration technique for high-accuracy 3d machine vision metrology using off-the-shelf tv cameras and lenses. *IEEE Journal of Robotics and Automation*, 3(4):323–344.

Tsai, R. (1987b). A versatile camera calibration technique for high-accuracy 3d machine vision metrology using off-the-shelf tv cameras and lenses. *IEEE Journal of Robotics and Automation*, 3(4):323–344.

Villa, Y., Araiza, M., Alaniz, D., Ivanov, R., and Ortiz, M. (2012). Transformation of phase to (x,y,z)-coordinates for the calibration of a fringe projection profilometer. *Opt. Laser Eng.*, 50(2):256–261.

Villaroman, N., Rowe, D., and Swan, B. (2011). Teaching natural user interaction using openni and the microsoft kinect sensor. In *Proceedings of the 2011 conference on Information technology education*, pages 227–232. ACM.

Vo, M., Wang, Z., Pan, B., and Pan, T. (2012). Hyper-accurate flexible calibration technique for fringe-projection-based three-dimensional imaging. *Opt. Express*, 20(15):16926–16941.

Wen, Y., Li, S., Cheng, H., Su, X., and Zhang, Q. (2010). Universal calculation formula and calibration method in fourier transform profilometry. *Appl. Opt.*, 49(34):6563–6569.

Xiao, Y., Cao, Y., and Wu, Y. (2012). Improved algorithm for phase-to-height mapping in phase measuring profilometry. *Appl. Opt.*, 51(8):1149–1155.

Xu, Y. and Zhang, S. (2012). Uniaxial three-dimensional shape measurement with projector defocusing. *Opt. Eng.*, 51(2):023604.

Yin, Y., Peng, X., Li, A., Liu, X., and Gao, B. Z. (2012). Calibration of fringe projection profilometry with bundle adjustment strategy. *Opt. Lett.*, 37(4):542–544.

Zappa, E. and Busca, G. (2009). Fourier-transform profilometry calibration based on an exhaustive geometric model of the system. *Opt. Lasers Eng.*, 47(7):754–767.

Zhang, S. (2016). *High-Speed 3D imaging with digital fringe projection techniques*. CRC Press.

Zhang, S. and Huang, P. S. (2006a). Novel method for structured light system calibration. *Opt. Eng.*, 45(8):083601.

Zhang, S. and Huang, P. S. (2006b). Novel method for structured light system calibration. *Optical Engineering*, 45(8):083601.

Zhang, Z. (2000). A flexible new technique for camera calibration. *IEEE Trans. Pattern Anal. Mach. Intell.*, 22(11):1330–1334.